

5. THE ARCTIC—M. O. Jeffries and J. Richter-Menge, Eds.

a. Overview—M. O. Jeffries and J. Richter-Menge

Calendar year 2011 was characterized by continuing change throughout the Arctic environmental system. A key driver of systemwide change is a $\sim 2^{\circ}\text{C}$ increase in annual mean surface air temperature since the mid-1960s, which is 1.5°C greater than (more than double) the temperature increases at lower latitudes. This chapter describes some of the systemwide changes in ten categories: Air temperature, atmospheric circulation and clouds; Ozone and UV radiation; Terrestrial snow; Glaciers and ice caps (outside Greenland); Greenland Ice Sheet; Permafrost; Lake ice; Sea ice; Ocean; and Ocean acidification. Some of the key events are summarized below.

Ozone concentrations in the Arctic stratosphere during March 2011 were the lowest ever recorded since 1979, and led to elevated surface UV levels throughout the Arctic and sub-Arctic.

Annually-averaged Arctic temperatures continued to show area-wide positive (warm) anomalies, relative to the end of the 20th century. There were multi-month-long shifts in the dominant wind pattern, responding to changes in the polar vortex, which affected the distribution of surface temperatures and snow and ice conditions. For example, warm air temperature anomalies over the Eurasian Arctic in spring 2011 resulted in a new record low June snow cover extent and spring snow cover duration, and earlier (by 10–30 days) lake ice break-up and shorter (by 14–21 days) ice duration. Conversely, penetration of Arctic air masses into northern and eastern Europe in autumn 2010 and spring 2011 caused earlier freeze-up and later break-up, respectively, and thus longer (by 28–42 days) lake ice duration.

On the Greenland ice sheet, below-normal summer snowfall, a decreasing trend in surface albedo, and elevated surface and upper air temperature anomalies resulted in a continued pattern of extreme surface melting and a negative mass balance. To the west, the mass loss from glaciers and ice caps in the Canadian Arctic was the greatest since GRACE (Gravity Recovery and Climate Experiment) satellite measurements began in 2002, continuing a negative trend that dates back to 1987.

Warm summer temperatures occurred in Alaska; Barrow, on the North Slope, experienced a record 86 consecutive days with minimum temperatures at or above freezing. New record high temperatures occurred at 20 m below the land surface at all permafrost observatories on the North Slope, where measurements began in the late 1970s.

Sea ice extent in September 2011 was the second lowest on record, while the extent of old ice (four and five years) reached a new record minimum that was only 19% of the mean for the period 1982–2005. For a second consecutive summer, the northern routes of the Northwest Passage and the Siberian Coast passage of the Northern Sea Route were open, and for a fourth consecutive summer, the southern route of the Northwest Passage was ice-free. An increase and decrease, respectively, in winter and summer cloud cover contributed to surface warming in the Arctic Basin and perhaps the near-record low sea ice extent.

Also responding to the near-record low sea ice extent in nearly all sectors of the Arctic Basin, upper ocean temperatures in summer 2011 were generally warmer than in the previous few summers. The sea surface temperature anomaly averaged over the Beaufort, Chukchi, East Siberian, Laptev, and Kara Seas was $+1.45^{\circ}\text{C}$, the highest since the historical maximum value ($+2.8^{\circ}\text{C}$) observed in 2007.

b. Air temperature, atmospheric circulation, and clouds—

J. Overland, U. Bhatt, J. Key, Y. Liu, J. Walsh, and M. Wang

The annual mean surface air temperature over Arctic land areas has experienced an overall warming of about 2°C since the mid-1960s (Fig. 5.1). In 2011, the annual mean air temperature was slightly warmer than in 2009 and 2010. The cooler temperatures in 2009 and 2010 reflected cold continents in winter, while Eurasia had warmer temperatures in spring 2011. Area-wide positive temperature anomalies (Fig. 5.2), which show systematic changes since the end of

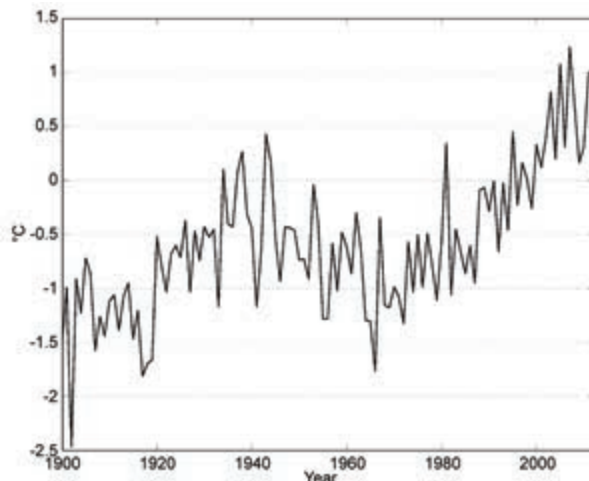


FIG. 5.1. Arctic-wide annual average surface air temperature anomalies relative to the 1961–90 mean, based on land stations north of 60°N . Data are from the CRUTEM 3v dataset at <http://www.cru.uea.ac.uk/cru/data/temperature/>. Note this curve does not include marine observations.

the 20th century, continued in 2011. Note the almost complete absence of negative temperature anomalies in Fig. 5.2. This temperature pattern is a manifestation of “Arctic amplification”, which is characterized by temperature increases 1.5°C greater than (more than double) the increases at lower latitudes (Overland et al. 2011a).

Spatial distributions of seasonal near-surface temperature anomalies (Fig. 5.3) were influenced by changes in the polar vortex, which is reflected in the sign and magnitude of the Arctic Oscillation index (AO; Table 5.1). A positive index corresponds to strong zonal wind flow, while a negative index corresponds to more meridional and spatially-variable flow. Table 5.1 indicates a large range in the magnitude of the AO in 2011; this has been characteristic of the AO since December 2009. It has been suggested that changes in the polar vortex are increasingly influenced by changes in Arctic surface characteristics, e.g., reduced sea ice and changes in snow cover, but these ideas are still highly controversial (Overland et al. 2011b).

The distinct shifts between large negative and positive phases of the AO index had a striking effect on the location of major warm and cold regional temperature anomalies in the Arctic and sub-Arctic throughout the year. Early winter 2011 saw a continuation of the negative AO Warm Arctic-Cold Continent pattern (Overland et al. 2011a) of the previous year, with warm temperatures lying north of far eastern Siberia and Alaska, in the vicinity of greater Baffin Bay and far northeastern Canada, and to some extent in the Kara Sea. Beginning in February, there was a major shift to a positive AO index, with cold temperatures in the Baffin Bay region and warmer anomalies developing in Eurasia due to westerly winds. A new record low June snow cover extent (since satellite observations began in 1966) occurred over Eurasia in 2011 (see section 5d) due to persistent warm spring air temperature anomalies over almost the entire Eurasian sector of the Arctic. In summer, when the AO shifted to a negative state, warm temperature anomalies returned to northern Canada with cool temperature anomalies in the Bering Sea. November and December had a strong positive AO pattern again, with warm anomalies in Eurasia and

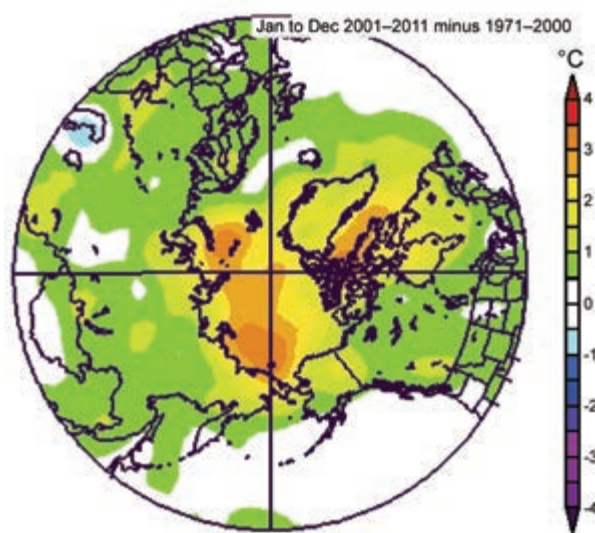


FIG. 5.2. Annual average near-surface (1000 hPa) air temperature anomalies (°C) for 2001–11 relative to the period 1971–2000. Data are from NOAA/ESRL, <http://www.esrl.noaa.gov/psd/>. (Source: NCEP/NCAR)

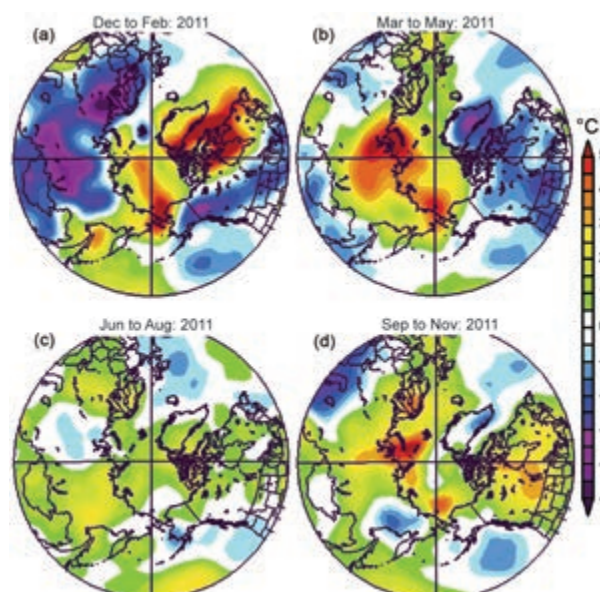


FIG. 5.3. Seasonal, near-surface (1000 hPa) air temperature anomalies (°C) in 2011 relative to the 1981–2010 baseline period. (a) Dec 2010–Feb 2011, (b) Mar–May 2011, (c) Jun–Aug 2011, and (d) Sep–Nov 2011. (Source: NCEP/NCAR)

TABLE 5.1. Monthly Arctic Oscillation Index for 2011 (from NOAA/CPC). Values are normalized by the standard deviation of the monthly index.

JAN	FEB	MAR	APR	MAY	JUNE	JULY	AUG	SEP	OCT	NOV	DEC
-1.68	1.57	1.42	2.27	-0.04	-0.86	-0.47	-1.06	0.66	0.80	1.46	2.22

western Canada, and cold anomalies in Greenland and eastern Asia.

The large negative values of the AO during summer 2011, and the associated wind pattern, represent an unusual event. Unlike summer climatology, which has generally weak winds confined to the Arctic, in July 2011 multiple low 850-hPa geopotential height centers formed in southerly locations along the continental rim of the Arctic Basin (Overland et al. 2011b). This provided the unusual warming in west Greenland during summer 2011 (similar to 2010), warm temperatures in Barrow, Alaska, cold temperatures in western Siberia, and kept warm storms from entering the Bering Sea. Barrow had a record (based on over 80 years of observations) 86 consecutive days with minimum temperatures at or above freezing beginning June 30. The previous record was 68 days set in 2009. For the sixth consecutive year, the first freeze of autumn in Fairbanks, Alaska, occurred more than two weeks later than its long-term average. Unlike 2007, when the wind pattern in every summer month contributed toward record sea ice loss in the Pacific Arctic via northward transport of ice and heat toward the North Pole, the near-record sea ice loss in September 2011 occurred despite a more variable wind circulation.

In 2011, Arctic cloud cover was somewhat higher than the average of the last 10 years (2002–11) in wintertime (January–March) and lower than average in the summer (June–August), particularly over the western Arctic Ocean. Figure 5.4 shows the cloud cover anomalies for representative winter and summer months. In spring and autumn, cloud cover was similar to the 10-year mean (not shown). The annual average cloud cover in 2011 over the Arctic Ocean was not significantly different from recent years. The 2011 wintertime increase and summertime decrease in cloud cover resulted in greater surface warming, as Arctic clouds generally have a warming effect in the winter and a cooling effect in the summer. This potentially contributed to the near-record low sea ice extent. This contrasts with the general trend over the period 1982–2004, when a decrease in wintertime and increase in springtime cloud cover over parts of the Arctic acted to dampen surface

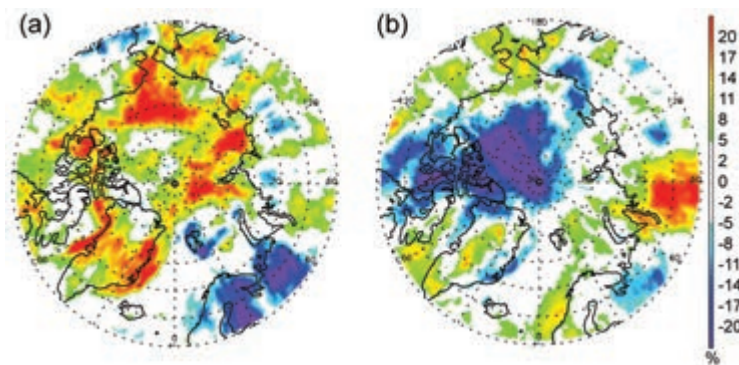


FIG. 5.4. Cloud cover anomalies (%) in (a) February and (b) July 2011 relative to the corresponding monthly means for the period 2002–11, based on data from the Moderate Resolution Imaging Spectroradiometer (MODIS) on the Aqua satellite.

warming (Wang and Key 2003, 2005). While clouds influence the surface energy budget (Y. Liu et al. 2009), they also respond to changes in the sea ice cover (Vavrus et al. 2011), as was evident in 2011. Figure 5.5 shows the cloud cover anomaly for the first half of September 2011, with higher-than-normal cloud cover in the poleward portions of the Beaufort, Chukchi, and Laptev Seas; sea ice concentration was lower than normal in these same areas (Fig. 5.5b). This is not coincidental, as a feedback analysis of data from 2000 to 2010 indicates that a 1% decrease in ice concentration leads to a 0.3–0.4% increase in cloud cover (Liu et al. 2012).

c. *Ozone and UV radiation*—G. Bernhard, G. Manney, V. Fioletov, J.-U. Grooß, A. Heikkilä, B. Johnsen, T. Koskela, K. Lakkala, R. Müller, C. L. Myhre, and M. Rex

Ozone concentrations in the Arctic stratosphere during March 2011 were the lowest since satellite records began in 1979 (Manney et al. 2011). The

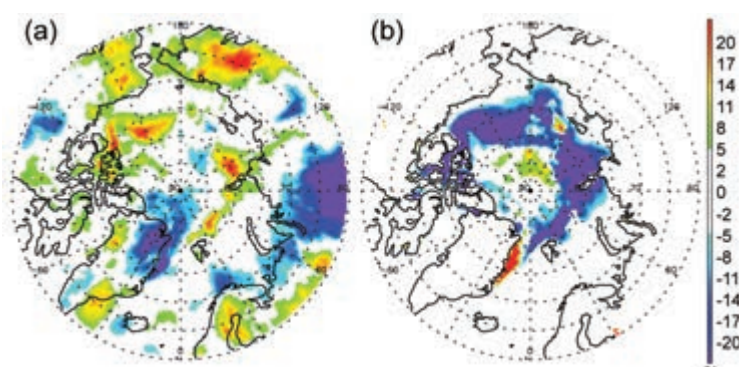


FIG. 5.5. (a) Cloud cover anomalies and (b) sea ice anomalies for September 2011 relative to the September mean for the period 2002–11. In both figures, the unit of anomaly is % above or below normal. Cloud cover is based on Aqua MODIS data. Sea ice concentration is from the Special Sensor Microwave/Imager (SSM/I) using the NASA team algorithm.

SIDE BAR 5.I: SOURCES OF ATMOSPHERIC CARBON DIOXIDE AND METHANE IN THE ARCTIC—E. J. DLUGOKENCKY AND L. BRUHWILER

Together, carbon dioxide (CO_2) and methane (CH_4) are responsible for ~80% of direct radiative forcing caused by long-lived greenhouse gases: 2.29 W m^{-2} out of 2.81 W m^{-2} in 2010 (update of Hofmann et al. 2006). Observations of CO_2 and CH_4 are of particular interest in the Arctic, where there are two potentially large reservoirs of carbon that are vulnerable and where land surface temperatures have been increasing and are projected to increase in the future (McGuire et al. 2009; O'Connor et al. 2010).

The first reservoir, methane-rich clathrate hydrates, occurs in sediments at the bottom of the Arctic Ocean. There is concern that rising ocean water temperatures, especially on the relatively shallow eastern Siberian Arctic continental shelf, will cause the clathrates to destabilize and release massive pulses of methane to the atmosphere (Kennett et al. 2000). However, measurements of CH_4 in ice cores (e.g., Severinghaus et al. 1998) do not support the idea that massive pulses of CH_4 from clathrates caused rapid climate warming in the past. It remains to be seen whether the climate response to current and future clathrate release will differ from previous records.

The second reservoir, Arctic permafrost, contains $\sim 1000 \text{ Pg C}$ ($\text{Pg C} = 10^{15} \text{ g carbon}$) in the top 3 m (Tarnocai et al. 2009), significantly more carbon than is currently in the atmosphere ($\sim 830 \text{ Pg C}$). As the Arctic warms and permafrost thaws, this ancient carbon can be released as either CO_2 or CH_4 . A recent review of the potential impacts of climate change in the 21st century on northern peatlands, much of it underlain by permafrost, suggests that both CO_2 and CH_4 emissions from this source will increase significantly in the future (Frolking et al. 2011).

Carbon dioxide and methane abundances from weekly samples collected at seven Arctic and sub-Arctic sites and Mauna Loa, Hawaii, are shown in Fig. SB5.1. High latitude CO_2 values are the same as at Mauna Loa, and all sites show a strong seasonal cycle superimposed on the long-term trend to higher values (Fig. SB5.1a). The seasonal cycle of CO_2 at high northern latitudes results from seasonal uptake (photosynthesis) and release (respiration) of carbon by the biosphere. The steep upward trend in CO_2 is due to global fossil fuel use.

Like CO_2 , the CH_4 records also have a seasonal cycle superimposed on a long-term trend to higher values (Fig. SB5.1b). Unlike CO_2 , the CH_4 record shows higher values at the Arctic and sub-Arctic sites than at Mauna Loa. The seasonal cycle at all sites is due to greater photochemical destruction of CH_4 in summer than in winter. However, photochemical destruction is slower at high latitudes. This, combined

with CH_4 transport from lower latitudes and a currently small contribution from high latitude sources, explains the greater CH_4 abundance at high latitudes. As the Arctic warms, contributions from local methane sources will likely increase, possibly by a large amount. However, to date, there is no evidence that natural emissions of CH_4 in the Arctic have increased significantly in the past decade (Bruhwiler and Dlugokencky 2011).

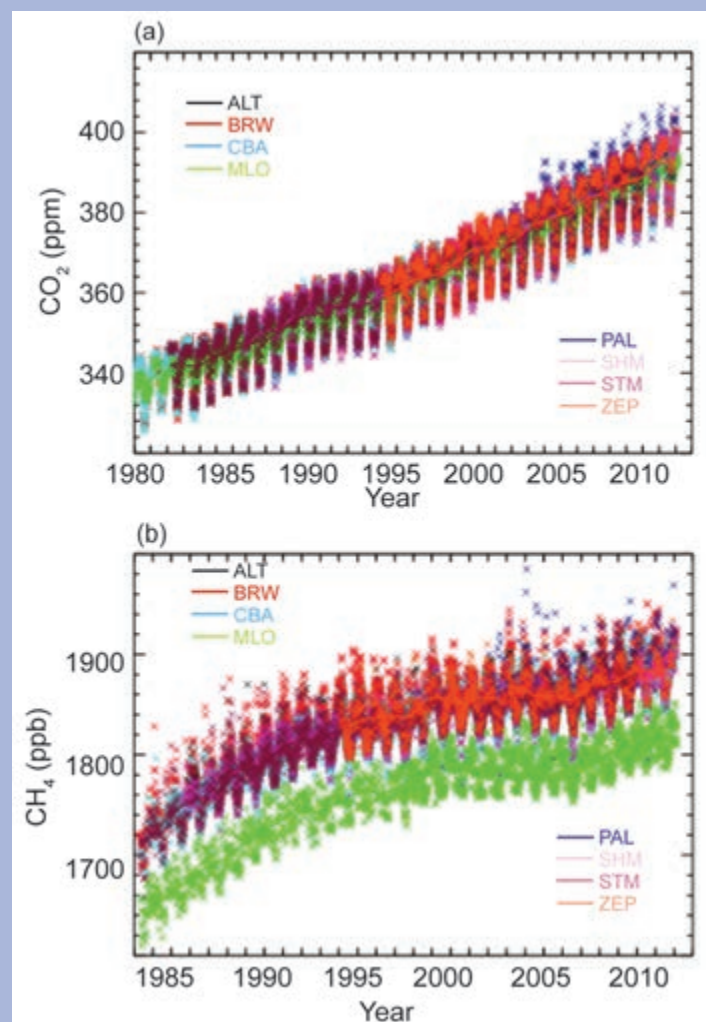


FIG. SB5.1. (a) CO_2 and (b) CH_4 dry air mole fractions from seven Arctic and sub-Arctic air sampling sites and from Mauna Loa Observatory (MLO), all in the NOAA ESRL air sampling network. The northern sites are Alert, Canada (ALT), Barrow, Alaska (BRW), Cold Bay, Alaska (CBA), Pallas, Finland (PAL), Shemya Island, Alaska (SHM), Summit, Greenland (STM), and Ny Ålesund, Svalbard, Norway (ZEP). Further information about the sites is available at http://www.esrl.noaa.gov/gmd/dv/site/site_table.html#ccg_surface.

minimum total ozone column for March 2011, averaged over the “equivalent latitude” (Butchart and Remsberg 1986) band 63°N – 90°N , was 297 DU (Dobson Units). The previous record low, 315 DU, was observed in 2000 (Fig. 5.6). The fraction of the Polar vortex with total ozone below 275 DU is typically near zero for March, but reached nearly 45% in March 2011. Minimum total ozone in spring 2011 was continuously below 250 DU for about 27 days, and occurred over a maximum area of about 2 000 000 km 2 . Record-low values (not illustrated) between 220 DU and 230 DU were reached in small regions of the vortex for about one week in late March 2011.

The ozone loss in spring 2011 was comparable to that observed during the annually-recurring “ozone hole” over the Antarctic. The record loss was mostly caused by chemical destruction of ozone, attributed to the existing stratospheric burden of ozone-depleting halogens and favored by an unusually prolonged cold period in the lower stratosphere in 2011. Low temperatures facilitate the formation of polar stratospheric clouds (PSC), which provide surfaces for heterogeneous reactions that activate stratospheric chlorine. The activated chlorine, in turn, destroys ozone rapidly in catalytic cycles. A good indicator of the potential for chlorine activation and ozone loss is the volume of air within the Polar vortex with temperatures below the PSC occurrence threshold (Rex et al. 2004). Temperatures below the threshold temperature for PSC formation of about -77°C existed between December 2010 and early April 2011. Under these conditions, over 80% of the ozone present in January, from about 18 km to 20 km altitude, had been chemically destroyed by late March (Manney et al. 2011).

The extraordinary situation in 2011 is illustrated in Fig. 5.7, which compares satellite measurements of total ozone column on 3 April 1981 (a year with a long-lasting and cold Polar vortex, and relatively low stratospheric chlorine concentrations), 3 April 2002 (long-lasting warm vortex, high total chlorine loading), and 3 April 2011 (long-lasting cold vortex, high chlorine). The figure emphasizes that chemical ozone loss resulting from chlorine activation is most effective in years when there is a long-lasting cold vortex, such as 2011.

The low levels of total ozone led to elevated UV levels

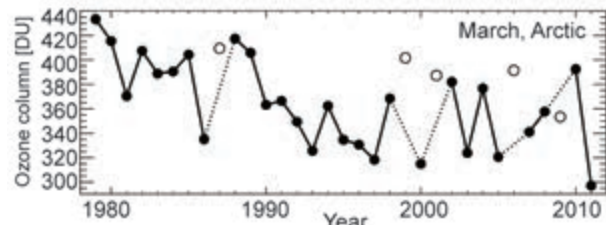


FIG. 5.6. Time series of area-averaged minimum total ozone for March in the Arctic, calculated as the minimum of the daily average column ozone poleward of 63°N equivalent latitude. Winters in which the polar vortex broke up before March (1987, 1999, 2001, 2006, and 2009) are shown as open symbols. Ozone in those years was relatively high because of mixing with air from lower latitudes. Figure adapted from Müller et al. (2008), updated using the combined total column ozone database of the New Zealand National Institute of Water and Atmospheric Research (NIWA), Version 2.7, provided by H. Chisholm of NIWA and G. Bodeker of Bodeker Scientific. The area-averaged minimum total ozone quantity is explained in Müller et al. (2008)

throughout the Arctic and sub-Arctic. Figure 5.8 illustrates the UV radiation in terms of the UV index, which is a measure of the ability of UV radiation to cause sunburn in human skin (WHO 2002). Changes in the UV index anti-correlate with changes in total ozone (compare 2011 data in center and bottom panels of Fig. 5.8). Noontime UV indices of March 2011 exceeded historical measurements for this month at all Arctic sites where ground-based UV monitoring systems are located (Bernhard et al. 2011). The maximum enhancement of the UV index relative to the climatological average was 122% (Fig. 5.8c). While these large relative changes are unprecedented, the absolute increases in UV levels were modest at all Arctic sites (e.g., increase by less than one UV index unit) because the low-ozone event occurred early in spring when the solar elevation was still small. Larger absolute increases of UV indices occurred at lower

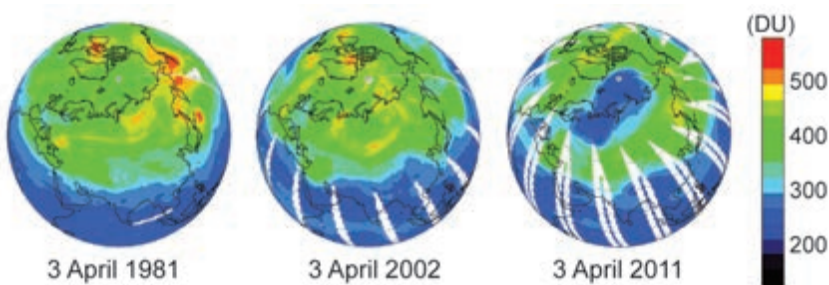


FIG. 5.7. Comparison of total ozone column (DU) measured by satellites on 3 April 1981, 2002, and 2011. Data are from the Total Ozone Mapping Spectrometer (TOMS) onboard the Nimbus-7 (1981) and Earth Probe (2002) satellites, and the Ozone Monitoring Instrument (OMI) onboard the AURA spacecraft (2011).

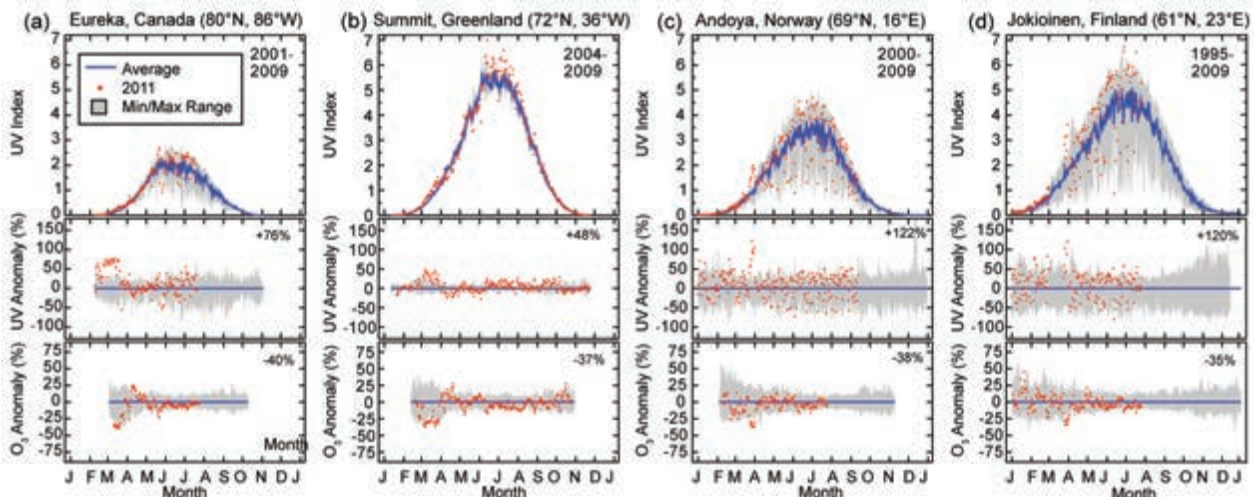


FIG. 5.8. Seasonal variation of the noontime UV Index for four Arctic and sub-Arctic sites measured by ground-based radiometers. The upper panel for each site compares the climatological average (blue line) with the measurements in 2011 (red dots), and historical minima and maxima (shaded range). The latter were calculated from measurements during the periods indicated in the top-right corner of the panel. The center panel shows the anomaly in the UV Index, calculated as the percentage departure from the climatological average. The numbers indicate the maximum anomalies for March and April 2011. The bottom panel shows a similar anomaly analysis for total ozone derived from measurements of the following satellites: TOMS/Nimbus-7 (1991–92), TOMS/Meteor-3 (1993–94), TOMS/EarthProbe (1996–2004), and OMI (2005–11). The shaded range for the ozone dataset is based on data for the years 1991–2009. Ozone data are available at <http://toms.gsfc.nasa.gov> and <http://ozoneaq.gsfc.nasa.gov>.

latitudes during excursions of the Polar vortex in April. For example, on 22 April, the clear-sky UV index over parts of Mongolia (48°N , 98°E) estimated by TEMIS (Tropospheric Emission Monitoring Internet Service at <http://www.temis.nl/uvradiation/UVindex.html>) was 8.6 when a lobe of the vortex extended to central Asia. The long-term average for this day at this location is 5.4 with a standard deviation of 0.5, i.e., the anomaly was more than six standard deviations larger than the climatological mean.

d. Terrestrial snow—C. Derksen and R. Brown

Time series of satellite-derived Arctic (land area north of 60°N , excluding Greenland) snow cover extent (SCE), snow cover duration (SCD), and snow water equivalent (SWE) anomalies (relative to a 1988–2007 base period) were calculated to place the 2010/11 snow season in the context of trends and variability during recent decades. Monthly SCE and seasonal SCD (computed separately for the first and second halves of the snow year) anomalies were computed from the weekly NOAA snow chart climate data record (CDR) maintained at Rutgers University and described in Brown and Robinson (2011). The SWE anomalies for 1980–2011 were calculated from an assimilation of surface observations of snow depth and satellite passive microwave measurements (Takala et al. 2011), the Canadian Meteorological Centre (CMC)

daily gridded global snow depth analysis (Brasnett 1999), and the ERA-interim atmospheric reanalysis (Dee et al. 2011a).

Air temperatures over the North American Arctic (NA) were below normal in April and early May, coincident with a strongly positive Arctic Oscillation (AO) (see Table 5.1), so SCE was above or near the long-term average during these months (Figs. 5.9a,b). When the AO shifted to a negative phase in May, the surface temperature anomalies became positive. By June, SCE anomalies over the NA sector of the Arctic were the second lowest on record (Fig. 5.9c). Unlike the slow start to the NA melt season, an extensive and persistent warm air temperature anomaly covered the Eurasian Arctic (EUR) through the entire spring season (see Fig. 5.3b), driving below-normal SCE in April and May, with a new record low June SCE over EUR since satellite observations began in 1966 (Fig. 5.9c).

Spatial patterns of seasonal SCD anomalies derived from the NOAA CDR for 2010/11 show an early spring melt anomaly located over the Ob and Yenisey basins (Fig. 5.9d) contributed to the shortest spring SCD for EUR in the NOAA snow chart record (Fig. 5.9f). A striking feature in the SCD anomaly time series is the seasonal asymmetry of the trends through the data record. The fall start date of snow cover over the Arctic has remained stable during the satellite era (Fig. 5.9e), in contrast to the trend

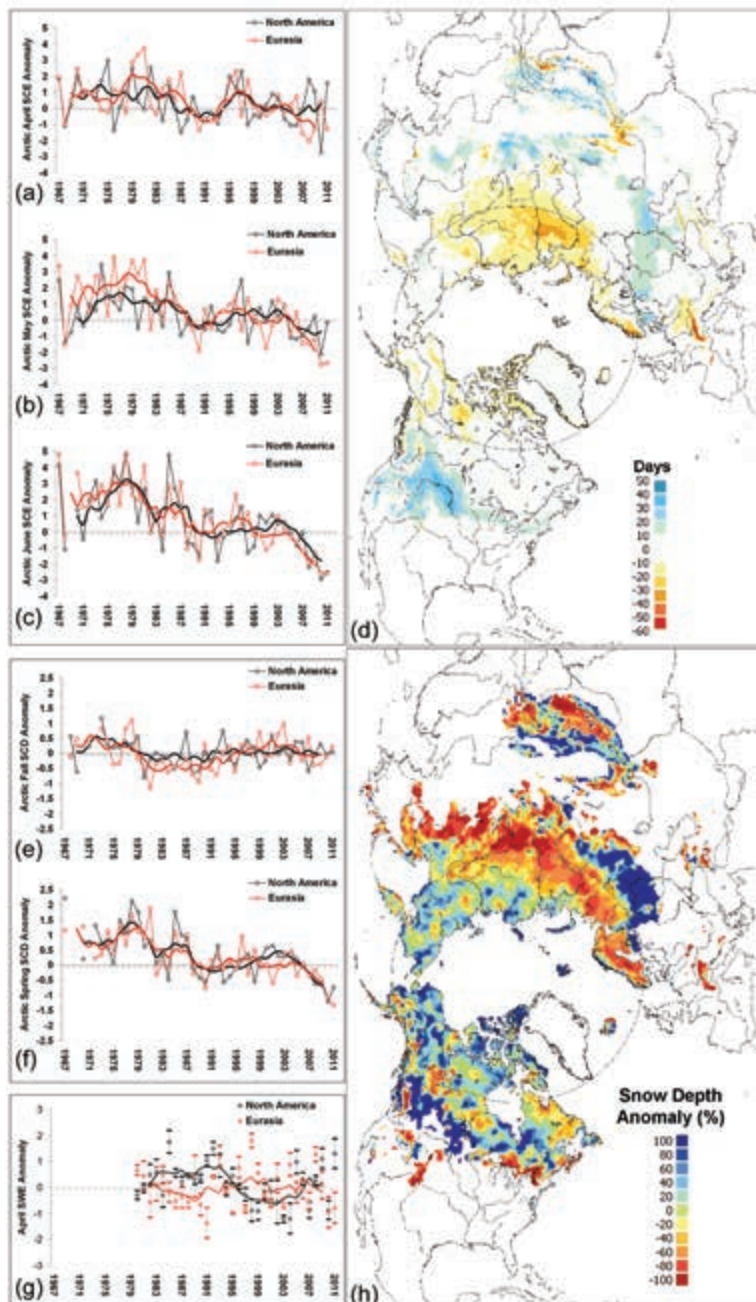


FIG. 5.9. (a)–(c) Monthly Arctic snow cover extent standardized (and thus unitless) anomaly time series (1988–2007 base period) from the NOAA snow chart CDR for (a) April, (b) May, and (c) June 1967–2011 (solid lines denote 5-yr moving average). (d) Snow cover duration (SCD) departures (1998–2010 base period) from the NOAA IMS data record for the 2011 spring season. (e)–(f) Arctic seasonal SCD standardized anomaly time series (1988–2007 base period) from the NOAA record for the first (fall) and second (spring) halves of the snow season (solid lines denote 5-yr moving average). (g) Time series of multidataset average monthly April snow water equivalent standardized anomalies (\pm the standard error) relative to 1988–2007 base period (solid lines denote 5-yr moving average). (h) April 2011 snow depth anomaly (% of 1999–2010 average) from the CMC snow depth analysis.

towards less snow in the spring period (Fig. 5.9f). The below-average Arctic SCE and SCD during 2011 is consistent with a decline in spring snow cover since the 1970s, identified from multiple datasets by Brown et al. (2010); the rate of this reduction has accelerated over the past five years.

The multi-dataset SWE anomaly series for the month of April is characterized by a high degree of interannual variability, with no significant trends (Fig. 5.9g). Across the NA Arctic, 2011 was characterized by the third highest April SWE anomaly in the record. This is also reflected in the mean April snow depth analysis from CMC (Fig. 5.9h), which shows predominantly positive snow depth anomalies over NA. Across EUR, the 2011 April SWE anomaly was near normal.

In summary, although peak SWE was close to average for EUR, and well above average for the NA Arctic, spring SCE and SCD during 2011 were below average across the Arctic because of warm air temperature anomalies during May and June. The observed reductions in spring SCE and SCD are consistent with the poleward amplification of snow cover sensitivity to warming air temperatures (Dery and Brown 2007). In spite of documented positive trends in observed precipitation over high latitudes (X. Zhang et al. 2007; Mekis and Vincent 2011), there is no evidence of pan-Arctic SWE trends when multiple datasets are considered.

e. Glaciers and ice caps (outside Greenland)—M. Sharp and G. Wolken

With an area of over 400 000 km², Arctic glaciers and ice caps are a significant contributor to global sea level change (Meier et al. 2007; Gardner et al. 2011; Jacob et al. 2012). Glaciers and ice caps gain mass by snow accumulation and lose mass by iceberg calving, surface melt, and runoff. The climatic mass balance (B_{clim} , the difference between annual snow accumulation and runoff) is an index of how they respond to cli-

mate change and variability. Note that B_{clim} is a new term (Cogley et al. 2011) synonymous with net mass balance (B_n) used in previous *State of the Climate* reports (e.g., Sharp and Wolken 2011a). Consistent with warming surface temperatures, the negative trend in B_{clim} of most Arctic glaciers and ice caps continues, albeit with regional variability.

At the time of writing, the only mass balance information available for 2010/11 is an estimate of -96 ± 49 Gt (which, in this case, is an estimate of the complete mass balance, ΔM , which includes mass losses by iceberg calving) for the Canadian Arctic Islands. Derived using GRACE satellite gravimetry, this is the most negative value for this region during the GRACE observation period, 2002–present (B. Wouters 2012, personal communication) and compares with the 2004–09 mean of -63 Gt yr^{-1} (Gardner et al. 2011). The large mass loss is consistent with very warm land surface and upper air (700 hPa) temperature anomalies due to anomalous meridional winds transporting heat into the region from the vicinity of southern Greenland, where anomalously warm sea surface temperatures occurred (Sharp and Wolken 2011b; sections 5b and 5f). In the previous balance year, 2009/10, the GRACE-derived ΔM estimate for this region was -73 ± 55 Gt (B. Wouters 2012, personal communication), confirming the growing

importance of glaciers and ice caps in the Canadian Arctic Islands as contributors to global sea level rise (Gardner et al. 2011).

At the time of writing, the most recent in situ measurements of B_{clim} for the twenty Arctic glaciers previously reported in the *State of the Climate* reports (e.g., Sharp and Wolken 2011a) are those for the 2009/10 balance year (World Glacier Monitoring Service 2011). The data (Table 5.2) show that all but one of the twenty glaciers had a negative climatic mass balance. Climatic mass balances of two of the four glaciers in Svalbard, including the one with a positive balance, were all less negative than the previous year. In Iceland, mass balances were all very negative, consistent with high summer air and sea surface temperature anomalies over Iceland and southern Greenland (Sharp and Wolken 2011b). Climatic mass balances of Alaskan glaciers were all negative, with very high mass loss occurring in the eastern Alaska Range (Gulkana). The climatic mass balances of the four glaciers in Arctic Canada were all negative, extending a period of very negative balances in the region that began in 1987 (Sharp et al. 2011).

f. Greenland ice sheet—M. Tedesco, J. E. Box, J. Cappellen, T. Mote, R. S. W. van de Wal, and J. Wahr

The duration of melting in 2011 was above average over much of Greenland, lasting up to ~30 days longer than the 1979–2010 average. Areas along the west and northwest coasts experienced the largest positive anomalies in the number of days when melting occurred (Fig. 5.10). The number of melting days in 2011 estimated from spaceborne passive microwave observations (Tedesco 2007) did not, however, break the previous record set in 2010 (Tedesco et al. 2011); 2011 ranked sixth, after 2010, 2007, 1998, 2002, and 2005.

The area of melt for the period June–August 2011 (Mote 2007) was the third greatest since records began in 1979, behind only 2007 and 2010. Note that the annual ranking is sensitive to the length of the season selected; expanding the season from 15 May to 15 September drops 2011 to the sixth most extensive melt year, following

TABLE 5.2. Annual (2009–10) climatic balances (B_{clim}) of 20 glaciers in the Arctic. Source: World Glacier Monitoring Service (2011).

Country	Glacier/Ice Cap	Latitude (°)	Longitude (°)	2009/10 B_{clim} (Kg m ⁻²)
Canada	Devon	75.42 N	83.25 W	- 417
	Meighen	79.95 N	99.13 W	- 387
	Melville South	75.43 N	114.99 W	- 939
	White	79.45 N	90.67 W	- 188
Iceland	Bruarjökull	64.67 N	16.17 W	- 1570
	Dyngjujökull	64.67 N	17.00 W	- 1540
	Eyjabakkajökull	64.65 N	15.58 W	- 1750
	Hofsjökull E	64.80 N	18.58 W	- 2830
	Hofsjökull N	64.95 N	18.92 W	- 2400
	Hofsjökull SW	64.72 N	19.05 W	- 3490
	Köldukvisljarjökull	64.58 N	17.83 W	- 2870
	Langjökull (South Dome)	64.62 N	20.30 W	- 3800
Norway (Svalbard)	Tungnáarárjökull	64.32 N	18.07 W	- 3551
	Austre Broggerbreen	78.88 N	11.83 E	- 440
	Hansbreen	77.08 N	15.67 E	- 14
USA (Alaska)	Kongsvegen	78.80 N	12.98 E	+ 130
	Midre Lovenbreen	78.88 N	12.07 E	- 200
	Gulkana	63.25 N	145.42 W	- 1832
	Lemon Creek	58.38 N	134.36 W	- 580
	Wolverine	60.40 N	148.92 W	- 85

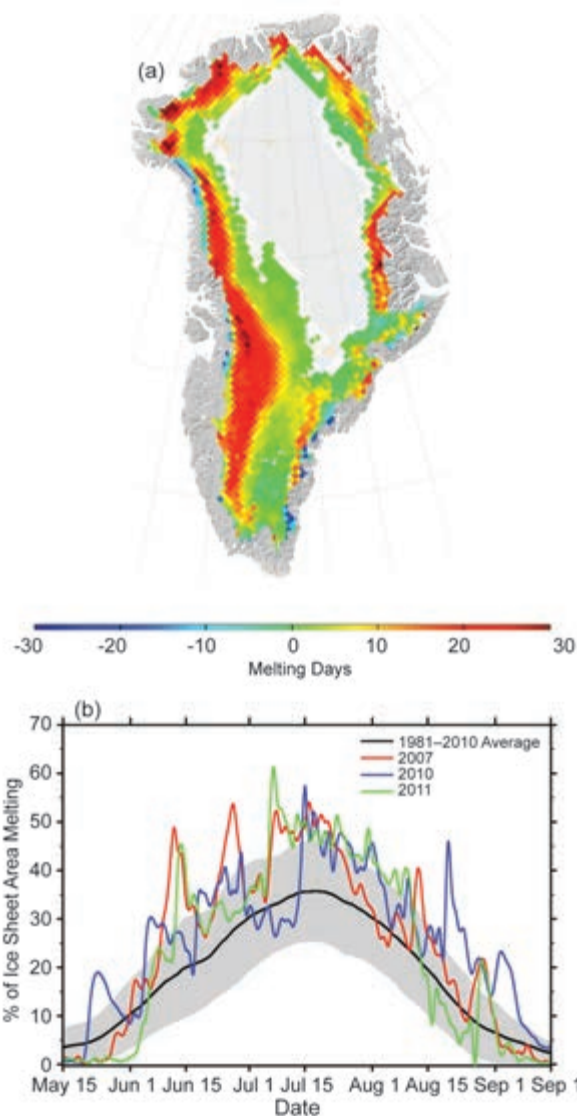


FIG. 5.10. (a) Map of the 2011 anomaly (relative to a 1979–2010 base period) for the number of melting days and (b) fractional area (%) of the Greenland ice sheet identified as melting by SSM/I (passive microwave). The standard deviation of the 1981–2010 base period is shaded.

2010, 2007, 2002, 1998, and 2005, in that order. The area subject to melting in summer 2011 was above the average (Fig. 5.10b), with an average value of 31% of the ice sheet area, compared to 33% in 2007 and 32% in 2010 (the 1981–2010 average is 24.1%). No other years since 1979 have had an average >30%. The linear trend for the area of the ice sheet subject to melting, updated to include 2011, is $16\,800 \text{ km}^2 \text{ yr}^{-1}$ ($R^2=0.58$). This indicates that, on average, in 2011 an area the size of Spain was subject to melting where no melting occurred in 1979.

In situ measurements of surface mass balance, and model estimates (Box et al. 2011), confirm the

extreme nature of melting in 2011 on the Greenland ice sheet. The weighted-average mass balance (-1.9 m w.e.) measured at the K-transect (in west Greenland near Kangerlussuaq; van de Wal et al. 2005) was the second lowest in 21 years of record and added to the cumulative mass loss that has been characteristic of this location since the late 20th century (Fig. 5.11). According to K-transect measurements, the equilibrium line elevation at the end of summer 2011 is estimated to be 1710 m above sea level (a.s.l.) compared to a value of ~ 1500 m a.s.l. in the early 1990s.

Over the entire Greenland ice sheet, estimates obtained by Gravity Recovery and Climate Experiment (GRACE; Velicogna and Wahr 2006) satellites indicate a cumulative loss of 422 Gt in 2011. This is 80% larger than the 2003–09 average annual loss rate of 233 Gt yr^{-1} (Fig. 5.12), the second largest annual loss rate in the GRACE record since observations began in 2003, and close to the 2010 record of 442 Gt.

Negative albedo anomalies estimated from the Moderate-Resolution Imaging Spectroradiometer (MODIS, the MOD10A1 product; Klein and Stroeve 2002) are widespread over the ice sheet during the 2011 melt period. MODIS data indicate a statistically significant decrease in the overall albedo of 0.055 during the 12-year period of record (Fig. 5.13a). The albedo anomaly map for summer 2011 (JJA) indicates large negative values, i.e., lower albedo, over west Greenland (Fig. 5.13b), where darker bare ice is exposed following the ablation of the previous winter's snow accumulation.

The extreme melting in 2011 is consistent with relatively warmer temperatures over Greenland (Cappelen et al. 2000, Cappelen 2011). During summer 2011, several ground stations recorded the warmest temperature since the beginning of records, e.g., Upernivik (records dating back to 1873) and Thule Air Force Base (records dating back to 1961; Box et al.

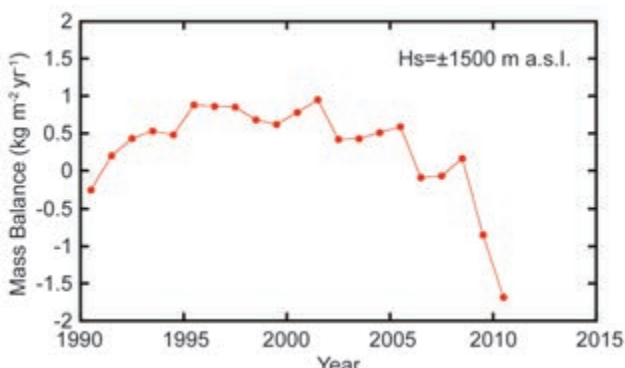


FIG. 5.11. The cumulative mass balance in the vicinity of the equilibrium line altitude ($H_s = \sim 1500 \text{ m a.s.l.}$, 67°N , 50°W) along the K-Transect of the Greenland ice sheet.

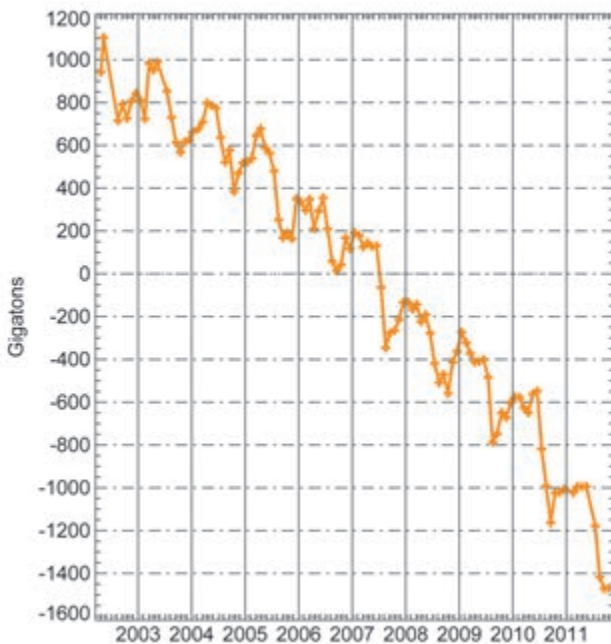


FIG. 5.12. Monthly unsmoothed values (+ symbols) of the total mass (Gigatons) of the Greenland ice sheet from GRACE. On the horizontal axis, each year begins on 1 January.

2011). Anomalously low temperatures were recorded during spring and autumn 2011. At Kangerlussuaq, April 2011 had the lowest temperature since records began in 1949. Consistent with ground observations, surface temperature estimated under clear sky conditions by MODIS (Wan et al. 2002; Wan 2008) since 2000 indicate an anomalously cold spring and an anomalously warm summer in 2011 (see section 5b for further description of these seasonal air temperature anomalies and the influence of atmospheric circulation).

MODIS data indicate statistically significant ice sheet surface warming in the past decade in both winter ($+3.1 \pm 1.9^\circ\text{C}$) and summer ($+1.8 \pm 0.7^\circ\text{C}$). Moreover, seasonally-averaged 2011 upper air temperature data available from twice-daily radiosonde observations (Durre et al. 2006) in the vicinity of Greenland support the ground- and MODIS-based surface temperature observations, indicating anomalous tropospheric warmth in summer and winter and mid-tropospheric cold anomalies in spring. Summer (JJA) 2011 had a persistent negative North Atlantic Oscillation (NAO) index, 2.4 standard deviations below the 1971–2000 summer average. This led to warm air advection from the south along the western coast, causing higher departures from normal summer temperature and drier-than-normal conditions in south Greenland. The Arctic Oscillation (AO)

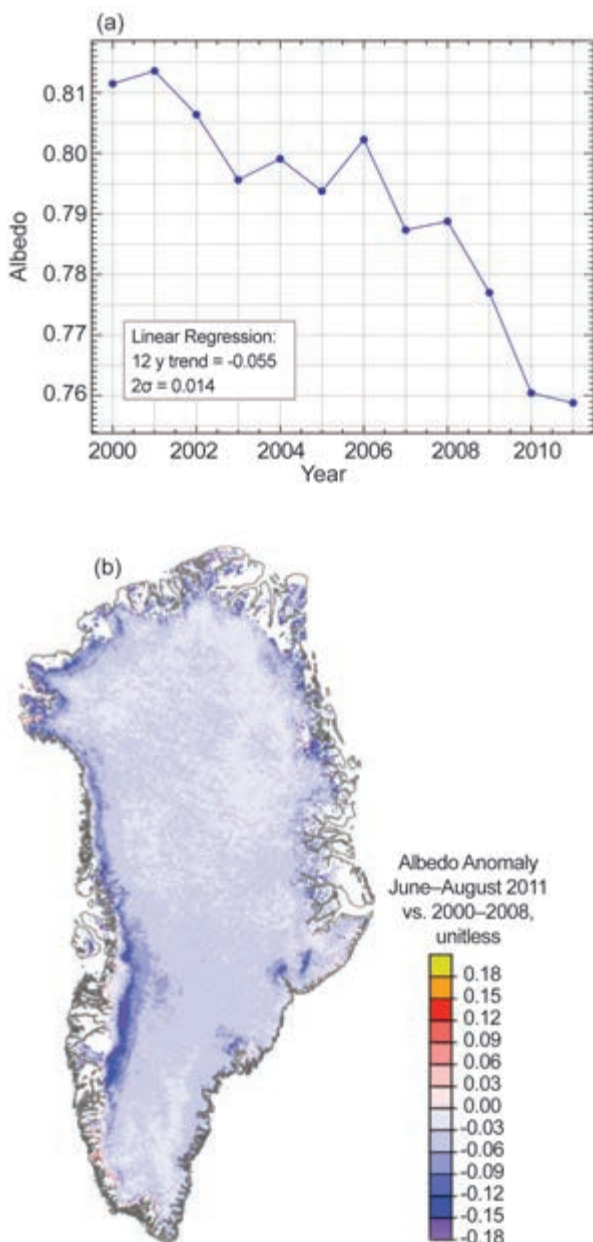


FIG. 5.13. (a) Greenland ice sheet albedo for the period 2000–11 and (b) summer (JJA) albedo anomaly in 2011 relative to the 2000–08 base period. Both (a) and (b) are derived from MODIS.

index was also persistently negative in summer 2011 (see Table 5.1).

A pattern of below-average precipitation for the period September 2010–August 2011 is evident at the west, southwest, and southeast stations of the Danish Meteorological Institute (Cappelen et al. 2000, Cappelen 2011), with the largest anomalies in the south (above one standard deviation). Conversely, in east and northeast Greenland, precipitation was above average (Box et al. 2011). According to measurements at the DMI stations, no annual precipitation

record was set in 2011. Although the melt season started late in 2011, dry and warm conditions, together with reduced accumulation caused a record bare ice exposure, which, in turn, enhanced the melt. At the south of the ice sheet, lower-than-normal winter accumulation allowed bare ice to appear earlier in the ablation zone.

g. Permafrost—V. E. Romanovsky, S. L. Smith, H. H. Christiansen, N. I. Shiklomanov, D. S. Drozdov, N. G. Oberman, A. L. Kholodov, and S. S. Marchenko

The most direct indicators of permafrost stability and changes in permafrost state are temperature and active layer thickness (ALT). A general increase in permafrost temperatures has been observed during the last several decades in Alaska (Osterkamp 2008; Smith et al. 2010; Romanovsky et al. 2010b), northern Canada (Smith et al. 2010), and Siberia (Romanovsky et al. 2010a).

At most Alaskan permafrost observatories there was substantial warming during the 1980s and especially in the 1990s (Fig. 5.14). The magnitude and nature of the warming varied spatially, but was typically from 0.5°C to 2°C at the depth of zero

seasonal temperature variation (Osterkamp 2008). However, during 2000–05, permafrost temperature was relatively stable on the North Slope of Alaska (Romanovsky et al. 2011; Smith et al. 2010; Fig. 5.14b), and there was even a slight decrease (ranging from 0.1°C to 0.3°C) in Interior Alaska during the last four years (Fig. 5.14c).

The most recent data may indicate that the coastal warming trend has propagated southward towards the northern foothills of the Brooks Range, where a noticeable warming in the upper 20 m of permafrost has become evident since 2008. In 2011, new record-high temperatures at 20 m depth were measured at all observatories on the North Slope, where measurements began in the late 1970s (Fig. 5.14b). Although these patterns of permafrost warming on the North Slope and a slight cooling in Interior Alaska are in good agreement with air temperature differences between the Arctic and the sub-Arctic, snow distribution variability may also have played a role.

In northwestern Canada, similar increases in cold permafrost temperature have been observed during the last 40 years (Burn and Kokelj 2009). Smaller increases in permafrost temperature have been ob-

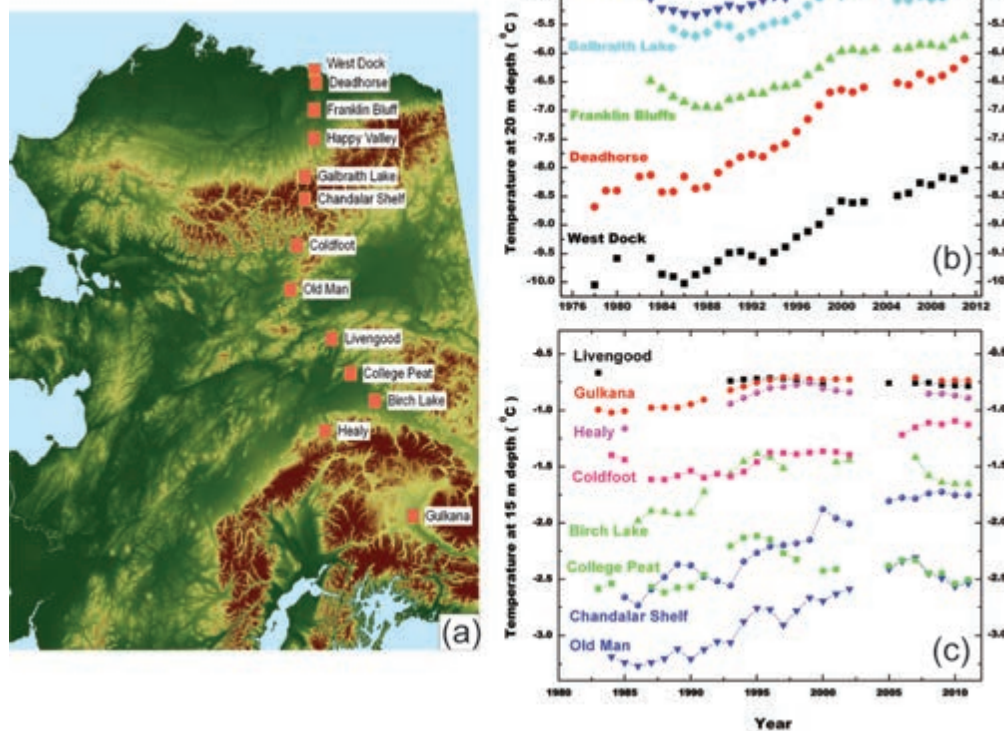


FIG. 5.14. (a) Location of sites where permafrost temperature was measured at (b) 20 m below the surface at locations from north to south across the North Slope of Alaska in the continuous permafrost zone, and (c) at 15 m below the surface in the Brooks Range and in interior Alaska. Note the higher permafrost temperatures in (c) interior Alaska than on the (b) North Slope due to the warmer climate of the interior.

served for warm permafrost in the discontinuous zone, with recent data indicating a negligible change (Romanovsky et al. 2011; Smith et al. 2010). In the high Canadian Arctic, greater warming has been observed, with recent data indicating a continuing steady increase in permafrost temperature since 2000 (Romanovsky et al. 2011; Smith et al. 2010). Permafrost temperature has increased by 1°C – 2°C in northern Russia during the last 30 to 35 years, but this trend was interrupted by colder conditions in summer 2009 and winter 2009/10 at many locations, especially in the western sector of the Russian Arctic. Long-term permafrost temperature records are limited for the Nordic area, with a few beginning at the end of the 1990s. These, however, show recent decadal warming of 0.04°C yr⁻¹ to 0.07°C yr⁻¹ in the highlands of southern Norway, northern Sweden, and Svalbard, with the largest warming in Svalbard and northern Scandinavia (Isaksen et al. 2011; Christiansen et al. 2010).

Identification of trends in ALT is difficult, as thaw depth responds to interannual variations in summer air temperature (e.g., Smith et al. 2009; Popova and Shmakin 2009). Decadal trends in ALT vary regionally, with a progressive increase in ALT observed

in some Nordic countries, e.g., in the Abisko area of Sweden since the 1970s, with an accelerated rate after 1995, and disappearance of permafrost in several mire landscapes (e.g., Åkerman and Johansson 2008; Callaghan et al. 2010). This increase ceased during 2007–10, coincident with drier summer conditions (Christiansen et al. 2010). ALT has increased since the late 1990s on Svalbard and Greenland, but the rates vary spatially and temporally (Christiansen et al. 2010). In the eastern Canadian Arctic, ALT has increased since the mid-1990s, with the largest increase occurring in bedrock of the discontinuous permafrost zone (Smith et al. 2010). Active-layer thickness on the North Slope of Alaska has been relatively stable, without pronounced trends during the last 15 years (Streletskiy et al. 2008; Shiklomanov et al. 2010).

h. Lake ice—C. R. Duguay, L. Brown, K.-K. Kang, and H. K. Pour

Lake ice phenology, which encompasses freeze-up (ice-on) and break-up (ice-off) dates, and ice cover duration (ICD), is largely influenced by air temperature changes and is therefore a robust indicator of regional climate (e.g. Duguay et al. 2006; Kouraev et al. 2007; Latifovic and Pouliot 2007). Ground-based observational records have provided evidence of later

SIDE BAR 5.2: CHANGING ARCTIC TUNDRA VEGETATION BIOMASS AND GREENNESS—D. A. WALKER, U. S. BHATT, H. E. EPSTEIN, P. BIENIEK, J. COMISO, G. V. FROST, J. PINZON, M. K. RAYNOLDS, AND C. J. TUCKER

Eighty percent of the non-alpine tundra biome in the Arctic is within 100 km of the Arctic Ocean and adjacent seas, its distribution largely controlled by cold summer air masses associated with the pack ice. It is expected that if sea ice continues to decline the adjacent tundra areas will warm during the summer (Lawrence et al. 2008), and the higher temperatures will increase tundra primary productivity and biomass (Bhatt et al. 2010; Elmendorf et al. 2011; Callaghan et al. 2011; Epstein et al. 2012).

Recently, Raynolds et al. (2012) established a very strong correlation ($r^2 = 0.94$, $p < 0.001$) between zonal (climax) above-ground plant biomass at the peak of the growing season at mesic (moist) sites and the annual maximum NDVI (Normalized Difference Vegetation Index). The latter is an index of vegetation greenness derived from Advanced Very High Resolution Radiometer (AVHRR) data. Derived for zonal/climax vegetation along two transects in North America and Eurasia, the Raynolds et al. (2012) relationship was used by Epstein et al. (2012) to determine that above-ground tundra biomass at representative sites increased by 19.8% during the period of the NDVI record (1982–2010). This has major implications for tundra ecosystems, including active layer depth, permafrost temperature and distribution, hydrology, wildlife, and human use of Arctic landscapes.

The biomass-greenness relationship described above offers the promise of easily determining total above-ground tundra biomass from NDVI. However, since the data were limited to vegetation on zonal sites, and it is not known how well the relationship holds for complex landscapes composed of many plant community types, NDVI continues to be used primarily as a measure of greenness and a proxy for total above-ground biomass.

During 30 years of AVHRR observations (1982–2011), area-averaged MaxNDVI (Fig. SB5.2b) has increased 15.5% in the North American Arctic, with a particularly sharp increase since 2005, and 8.2% in the Eurasian Arctic, although values have been nearly constant since 2001 (Bhatt et al. 2010, updated to 2011). Summer land temperatures in the tundra regions also show different geographic patterns between 1982 and 2011, with the area-averaged Summer Warmth Index (SWI, the sum of mean monthly temperatures $> 0^\circ\text{C}$, or thawing degree months) increasing 10.1% for North America and decreasing 2.6% for Eurasia (Fig. SB5.2a). Large areas of the Eurasian Arctic are apparently cooling during the summer growing season and contributing to the smaller NDVI response. A decreasing NDVI trend is particularly pronounced in the region adjacent to the northern Barents and Kara Seas (Fig. SB5.2b), where an increase in extent and persistence of the open water sea-

freeze-up and earlier break-up dates in the Northern Hemisphere, particularly during the second half of the 20th century (e.g., Brown and Duguay 2010). In the last 20 years, however, ground-based lake ice networks have been diminished to the point where they can no longer provide the quality of observations necessary for climate monitoring. Satellite remote sensing is the most logical alternative for Arctic-wide lake ice observing.

Spatial and temporal variability in ice phenology and ICD derived at the pixel level from the NOAA Interactive Multisensor Snow and Ice Mapping System (IMS) 4-km resolution grid daily product (National Ice Center 2008) was analyzed for the 2010/11 ice season and compared to average conditions for the full length of the available satellite historical record (since 2004). The IMS incorporates a wide variety of satellite imagery (AVHRR, GOES, SSMI, etc.) as well as derived mapped products (USAF Snow/Ice Analysis, AMSU, etc.) and surface observations (see Helfrich et al. 2007 for details).

Freeze-up in 2010 was close to the 2004–10 mean throughout much of the Arctic. The major exception was northern and eastern Europe, where freeze-up occurred 20–40 days earlier than mean freeze-up. The

most likely explanation for this very early freeze-up is penetration of cold air from the Arctic into Europe in autumn 2011 (see section 5b).

Break-up in 2011 was close to the 2004–10 mean in the North American Arctic. In contrast, a large number of lakes in northernmost Europe and eastern Siberia experienced earlier break-up (10–20 days), while lakes in much of eastern Europe and the southern portion of northern Europe experienced later break-up (10–30 days). The earlier break-up in eastern Siberia is consistent with the record-low June snow cover extent (see section 5d) over Eurasia. The later break-up in eastern Europe and the southern portion of northern Europe is consistent with colder early spring temperatures in this region (see section 5b).

Compared to the 2004–10 mean, ICD (Fig. 5.15) in 2010/11 was ~14 days shorter in central and eastern Arctic Canada and 14–21 days shorter in eastern Siberia. In contrast, ICD was 14–21 days longer in Baffin Island and western Canada/Alaska and as much as 28–42 days longer in northern and eastern Europe. The combination of earlier freeze-up and later break-up due to colder winter/early spring weather explains the longer ICD over Europe.

son in the summer and into the fall could be providing a winter-long source of moisture to these areas, increasing winter snowpack and decreasing winter temperatures (Cohen et al. 2012).

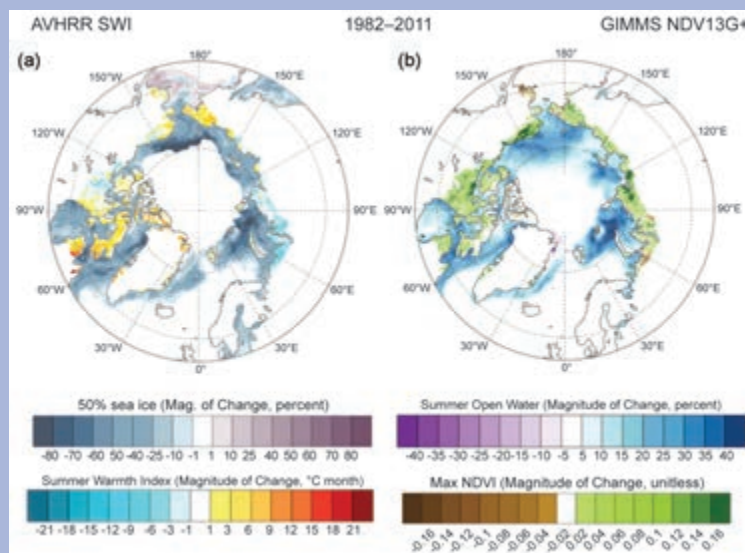


FIG. SB5.2. (a) Magnitude of changes in sea ice break-up (as represented by 50% sea ice concentration) and Summer Warmth Index for land area. **(b)** Magnitude of changes in summer (May–Aug) open water and tundra MaxNDVI (annual maximum NDVI, usually reached in early August). Magnitude of change is the slope of the simple linear regression trend line multiplied by the number of years of record (30 years: 1982–2011). The sea ice concentration and open water data were derived from SMMR and SSM/I passive microwave records. Ice concentration time series were assembled using data averaged over a three-week period centered on the week when mean concentrations were 50%; the more negative the value on the scale, the earlier 50% ice concentration, or break-up, occurs. Open water indicates the integrated summer open water amount. All the above information was derived from AVHRR data and the Global Inventory, Modeling and Mapping Studies (GIMMS) dataset.

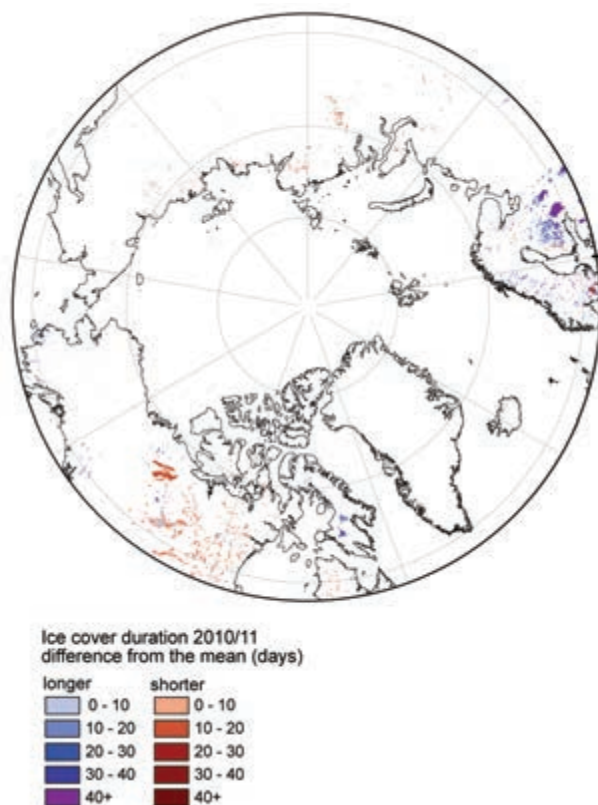


FIG. 5.15. Ice cover duration anomalies (days) in 2010–11 relative to the 2004–10 mean from the NOAA IMS 4-km product.

i. **Sea ice cover**—D. K. Perovich, W. Meier, J. Maslanik, and J. Richter-Menge

Sea ice extent is the primary variable for summarizing the state of the Arctic sea ice cover. Passive microwave instruments on satellites have routinely and accurately monitored the extent since 1979. There are two months that define the annual cycle and thus are of particular interest: March, at the end of winter, when the ice is at its maximum extent, and September, at the end of summer, when the ice reaches its minimum extent. Maps of ice extent in March 2011 and September 2011 are presented in Fig. 5.16.

As reported by the National Snow and Ice Data Center, on 9 September 2011, sea ice extent reached a minimum for the year of 4.3 million km². The 2011 minimum is the second lowest, only 0.2 million km² greater than the 2007 record minimum (<http://nsidc.org/arcticseainews/>) and 31% (2.1 million km²) smaller than the 1979–2000 average. The last five summers (2007–2011) have experienced the five lowest minima in the satellite record, and the past decade (2002–11) has experienced nine of the ten lowest minima.

Maximum sea ice extent in 2011 occurred on 7 March and was 14.6 million km². While the date of maximum extent was about normal compared to the 1979–2000 average, the ice extent itself was 7.7% less than the 1979–2000 average of 15.9 million km².

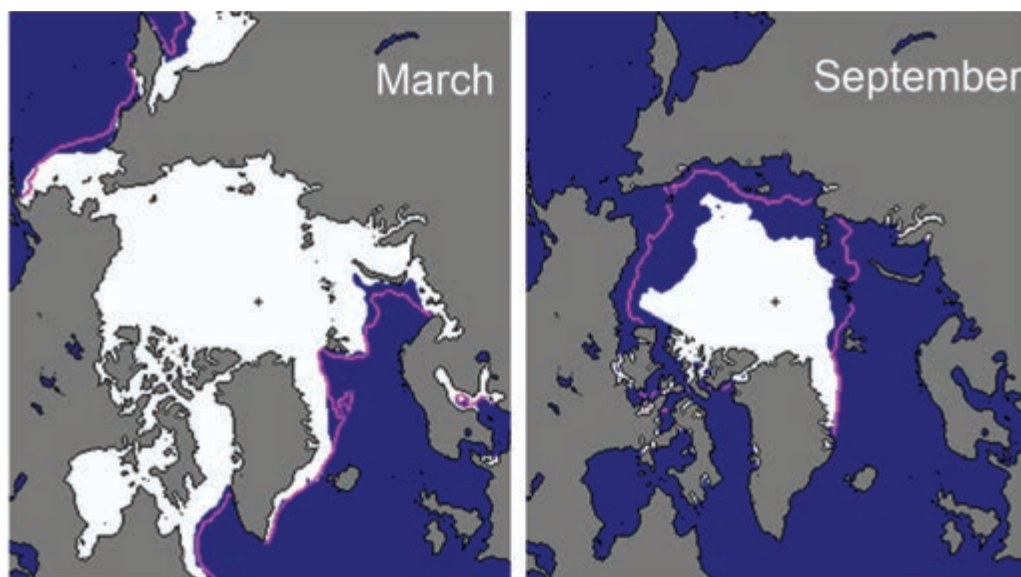


FIG. 5.16. Sea ice extent in March 2011 (left) and September 2011 (right), illustrating the respective monthly winter maximum and summer minimum extents. The magenta line indicates the median maximum and minimum ice extents in the given month for the period 1979–2000. Maps are from the National Snow and Ice Data Center Sea Ice Index, http://nsidc.org/data/seacie_index.

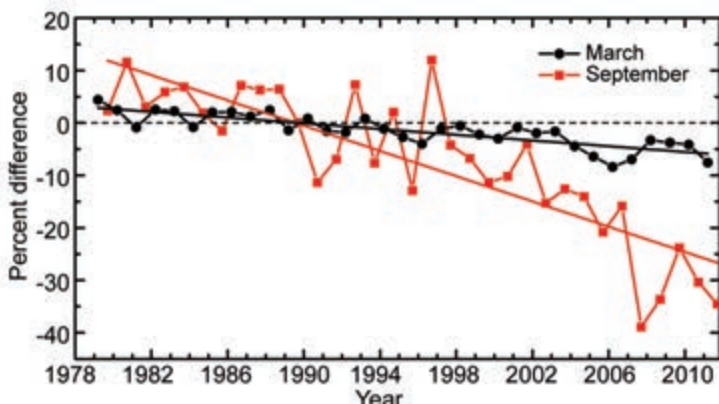


FIG. 5.17. Time series of the percentage difference in ice extent in March (the month of ice extent maximum) and September (the month of ice extent minimum) relative to the 1979–2000 base period. Based on a least squares linear regression (straight sloping red and black lines) for the period 1979–2011, the rate of decrease for the March and September ice extents is $-2.7\% \text{ decade}^{-1}$ and $-12.0\% \text{ decade}^{-1}$, respectively. Data are from the National Snow and Ice Data Center.

The time series of the anomalies in monthly average sea ice extent in March and September for the period 1979–2011 are shown in Fig. 5.17. The anomalies are computed with respect to the 1979–2000 base period. The large interannual variability in September ice extent is evident. Both winter and summer ice extent exhibit a negative trend, with values of $-2.7\% \text{ decade}^{-1}$ for March and $-12.0\% \text{ decade}^{-1}$ for September over the period of record.

Monthly ice extents averaged for the periods 1979–2000 and 2001–11 are shown in Fig. 5.18. Ice extents for the 2001–11 average are lower than the 1979–2000 average for all months, and for most months the curves are more than one standard deviation apart. The decline in ice extent is greatest in August, September, and October, and those months also show an increase in interannual variability for the 2001–11 period. The difference in ice extent between these two periods suggests a shift to a new regime of reduced sea ice.

The recent pronounced decrease in the extent of the September sea ice cover has been accompanied by large changes in its spatial distribution compared to 1980 (Fig. 5.16; for more details see figure SIO4 in Perovich et al. 2011). In 2011, there was a pronounced retreat of ice around the periphery of the Arctic basin and ice loss in the Ca-

nadian Arctic Archipelago (CAA), similar to the pattern of ice distribution observed in the past three years. Ice remains in the central Arctic, along northeast Greenland, and adjacent to the northern edge of the CAA. North of Alaska and Siberia, the ice edge forms an arc with lobes of ice extending from both edges. These lobes consist of a mixture of dispersed floes of first-year and multiyear ice amid considerable amounts of open water. This contrasts with many earlier years, including 2007, when the ice edge at the end of summer was compact and most of the remaining ice was a consolidated pack.

Further evidence of the dramatic reduction in the extent of the summer sea ice cover is the conditions in the southern and northern routes of the Northwest Passage and the Siberian Coast passage of

the Northern Sea Route. All three routes have been open (i.e., appeared ice-free in the passive microwave imagery) the past two years and the Northwest Passage southern route has been open every year since 2007. Additional information on the routes and on sea ice in the Greenland and Baltic Seas is available from the International Ice Charting Working Group news release (IICWG 2011).

The age of the ice is another key descriptor of the state of the sea ice cover. Older ice tends to be thicker

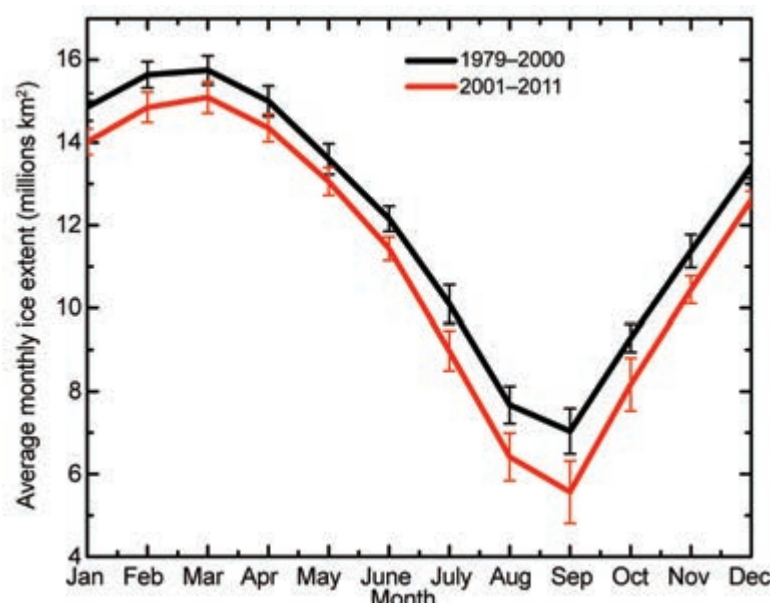


FIG. 5.18. Mean monthly sea ice extent for the periods 1979–2000 (black line) and 2001–11 (red line). The vertical bars represent one standard deviation about the mean.

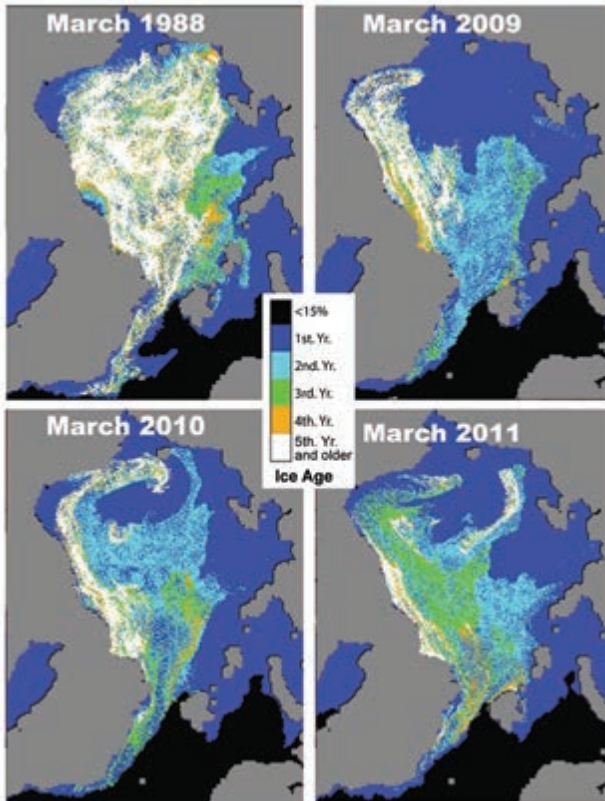


FIG. 5.19. Sea ice age in the first week of March derived from tracking the drift of ice floes in 1988, 2009, 2010, and 2011. Figure courtesy of J. Maslanik and C. Fowler.

and thus more resilient than younger ice. The age of the ice is determined using satellite observations to track ice parcels over several years. This method has been used to provide a record of ice age since the early 1980s. Figure 5.19 shows sea ice age derived from tracking ice parcels from 1979 through 2011. The distribution of ice of different ages illustrates the extensive loss in recent years of the older ice types (Maslanik et al. 2011). Analysis of the time series of areal coverage by age category indicates that the loss of the older (4- and 5-year ice) which began in earnest in 2005 (Maslanik et al. 2011) has continued, reaching a record minimum in summer 2011 of only 19% of the

1982–2005 mean. There is some recovery of third-year ice coverage from 2010 to 2011. The net increase in third-year ice from 2010 to 2011 (0.36 million km²) is greater than the decrease in 4+ year ice (-0.11 million km²), which suggests a potential gain in ice mass within the multiyear ice cover. However, given that the older ice types tend to be thicker (e.g., Maslanik et al. 2007), this increase might be relatively slight.

- j. *Ocean*—A. Proshutinsky, M.-L. Timmermans, I. Ashik, A. Beszczynska-Möller, E. Carmack, I. Frolov, R. Ingvaldsen, M. Itoh, T. Kikuchi, R. Krishfield, F. McLaughlin, H. Loeng, S. Nishino, R. Pickart, B. Rabe, B. Rudels, I. Semiletov, U. Schauer, N. Shakhova, K. Shimada, V. Sokolov, M. Steele, J. Toole, T. Weingartner, W. Williams, R. Woodgate, M. Yamamoto-Kawai, and S. Zimmerman

I) WIND-DRIVEN CIRCULATION

In 2011, the annual wind-driven circulation regime was anticyclonic (clockwise; Fig. 5.20, left panel), with an enlarged and well-organized Beaufort gyre (BG) and strong outflow of sea ice and surface fresh water via Fram Strait to the Greenland Sea. The Transpolar Drift, in its conventional definition, did not exist in 2011. Instead, it split into two branches and sea ice and fresh water in Fram Strait mainly originated from the Kara Sea and partly from the Lincoln Sea. Sea ice and surface waters from the Laptev Sea were largely swept into the BG. Near-surface waters and sea ice from the Chukchi and East Siberian Seas were driven westwards by winds, closing the large-scale circulation cell of the BG in the Canada Basin (Fig. 5.20).

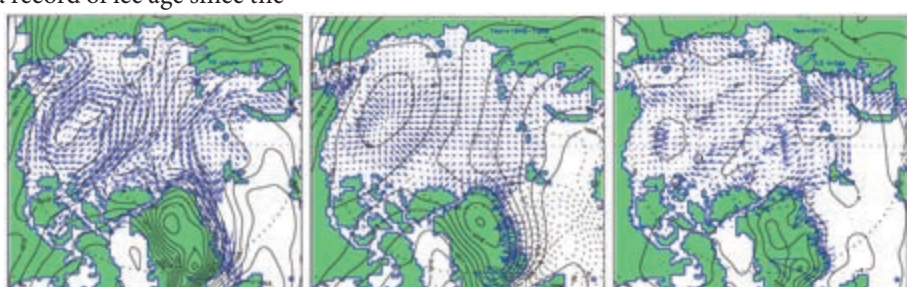


FIG. 5.20. (left) Simulated wind-driven ice motion (arrows) and observed sea level atmospheric pressure (hPa, black lines) for 2011. Results are from a 2D coupled ice-ocean model (Proshutinsky and Johnson 1997, 2011) forced by wind stresses derived from 2011 NCEP/NCAR reanalysis 6-hourly sea level pressure fields. (middle) Ekman transport (vectors, m² s⁻¹) and sea level pressure (SLP) averaged over 1948–88 showing typical climatic conditions: relatively fresh waters from the entire Arctic Ocean are accumulated in the Beaufort Gyre (BG) region via Ekman transport. (right) 2011 Ekman transport and SLP anomalies relative to 1948–88 climatic conditions. In 2011, SLP over the BG region was somewhat lower than climatology while the accumulation of freshwater increased. The right panel also suggests that the increase of freshwater content in the BG region could originate from local sources.

A large-scale anticyclonic circulation regime (similar to that shown in Fig. 5.20, left panel) persisted between 1997 and 2011, with only one short-lived reversal to a cyclonic regime in 2009. The anticyclonic regime has dominated for at least 15 years, instead of the typical 5–8 year pattern reported by Proshutinsky and Johnson (1997, 2011). It may be that after the anomalous 2007 conditions (a historical minimum September sea ice extent and maximum upper-ocean warming and freshening), the Arctic climate system shifted towards a new pattern characterized by a more persistent anticyclonic regime and with relatively small changes from year to year. On the other hand, a comparison of sea level pressure and Ekman transport shows that the mean fields for 1948–88 (Fig. 5.20, center panel) and 1948–2011 (not shown) are essentially identical, implying that the climate (using a conventional definition of 30-year averaged fields) of ocean dynamics is stable, but that strong interannual and decadal variability exists.

2) OCEAN TEMPERATURE AND SALINITY

(i) Upper ocean temperature

Upper ocean temperatures in summer 2011 (Fig. 5.21) were generally warmer than in the previous few summers, in keeping with stronger sea ice melt, which occurred in nearly all sectors of the Arctic Ocean (see Figs. 5.16, 5.17). The sea surface temperature (SST) anomaly averaged over the Beaufort, Chukchi, East Siberian, Laptev, and Kara Seas was +1.45°C, the highest since the historical maximum value (+2.8°C) observed in 2007 (Steele et al. 2008).

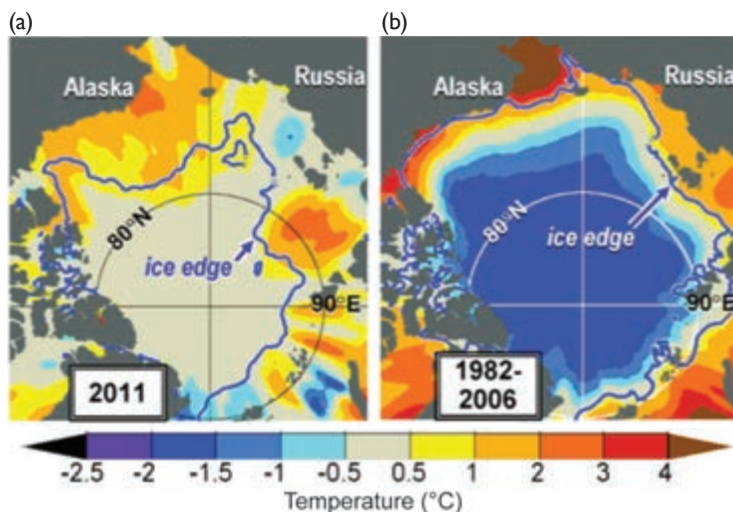


FIG. 5.21. (a) Summer (Jun–Sep) SST anomalies ($^{\circ}$ C) in 2011 relative to (b) the summer 1982–2006 base period. The anomalies are derived from satellite data according to Reynolds et al. (2002). The September mean ice edge (thick blue line) is also shown.

Partitioning this warming into that found in the western Arctic (Beaufort and Chukchi Seas) versus the eastern Arctic (East Siberian, Laptev, and Kara Seas), the distribution of warming in 2011 was very similar to that in 2007, i.e., about 60% western and 40% eastern. During the intervening cooler years, the partition was more heavily biased toward the western Arctic. Interannual variations in SST anomalies reflect differences in the pace of sea ice retreat, as well as changing advection of warm ocean currents from the south (Steele et al. 2010). In recent years, solar radiation has penetrated more easily into the upper ocean under thinning and retreating ice cover to create warm near-surface temperature maxima (Jackson et al. 2010, 2011).

(ii) Upper-ocean salinity

Relative to the 1970s Environmental Working Group climatology of the Arctic Ocean (Timokhov and Tanis 1997, 1998), the major upper-ocean salinity differences in 2011 (Fig. 5.22) are saltier central Nansen and Amundsen basins and a fresher Canada Basin, with the maximum freshwater anomaly centered in the BG. Another key feature of the upper ocean salinity, relative to climatology, is that the upper ocean is generally saltier around the southern boundary of the Canada Basin due to intensified upwelling at the basin boundaries associated with the large-scale wind-driven circulation in 2011 (Fig. 5.20, left panel). This circulation pattern shifted the position of the upper-ocean front between saltier waters of the Eurasian Basin and fresher Canada Basin

waters. The magnitude of salinity difference from climatology is less than 1 in the Barents Sea, much smaller than in regions of the central Arctic Basin. Upper-ocean salinity in 2011 is fresher than 1970s climatology on the south side of the Barents Sea Opening (BSO) and to the east of Svalbard, while areas of the central Barents Sea and to the north of Svalbard exhibit higher salinity.

In 2011, the magnitude of the freshwater content in the BG region was comparable to 2008–10 conditions, with the exception that freshwater tended to spread out from the 2007–09 BG center due to some reduction of Ekman pumping. In total, during 2003–11, the BG region accumulated more than 5000 km³ of freshwater; a

gain of approximately 25% (update to Proshutinsky et al. 2009) relative to climatology of the 1970s.

(iii) The Atlantic water layer

Warm water of North Atlantic origin, the Atlantic Water Layer (AWL), resides at depths between approximately 200 m and 900 m [less in the vicinity of Fram Strait (FS)] and is characterized by temperatures greater than 0°C and salinities greater than 34.5. In 2011, AWL maximum temperature anomalies (relative to 1970s climatology) were generally highest on the Eurasian side of the Lomonosov Ridge, with maximum anomalies greater than +2°C in FS (Fig. 5.22). Warming was less pronounced in the Canada Basin than in the Eurasian Basin. There was little to no temperature anomaly (< 0.1°C) at the south-east boundary of the Canada Basin or in the basin boundary regions adjacent to Greenland and the CAA. Negative (cooling) temperature anomalies were observed in the vicinity of Nares Strait.

The characteristics of the AWL are regulated by the Atlantic water inflow through Fram Strait and via the BSO. After reaching a maximum in 2006 (Fig. 5.23), AWL temperature and salinity in FS have been decreasing and increasing, respectively. In summer 2010, AWL temperature returned to the long-term mean (2.7°C). The autumn and winter AWL temperatures were slightly lower in 2010/11 than the previous year, while in summer 2011 the mean temperature remained close to that observed in 2010. In summer 2011, an anomalously warm and saline southward flow of AWL was observed in the western FS (not shown). This may indicate that the warm AWL anomaly, which had entered the Arctic Ocean in 2006, has returned to FS after completing a loop in the Eurasian Basin.

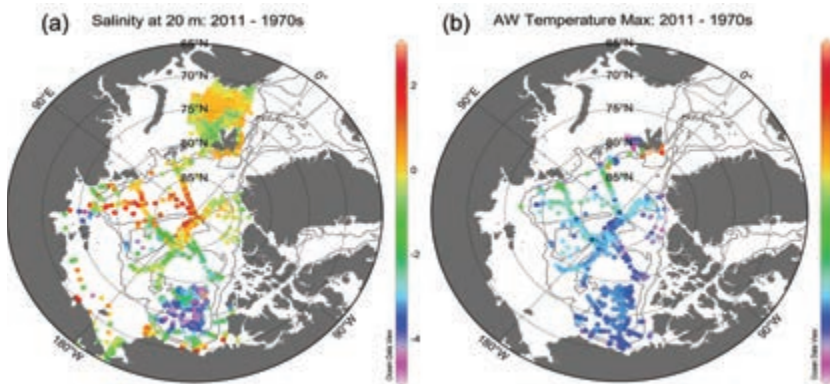


FIG. 5.22. (a) Anomalies of upper-ocean salinity at 20-m depth in 2011 relative to 1970s climatology (see Proshutinsky et al. 2011b, figure O.3). **(b)** Atlantic Water Layer (AWL) temperature maximum anomalies (°C) in 2011 relative to 1970s climatology (see Proshutinsky et al. 2011b; Fig. 5.6). Contour lines show the 500-m and 2500-m isobaths.

The volume flux via the BSO (Fig. 5.23) was low in 1997–2002 and then relatively high in 2003–06. In 2006, the volume flux was at a maximum in winter and very low during fall. After 2006, the inflow has been relatively low, in particular during spring and summer months. A weak increasing trend in volume transport has been observed since 2009, and the volume flux in 2011 was close to the 1997–2011 mean. The AWL temperature in the BSO (Fig. 5.23) varies asynchronously with water transport, and has been declining since 2006. Thus, since 2009 the temperatures have decreased while the volume flux has increased slightly.

(iv) The Pacific water layer

The Pacific Water Layer (PWL) is located in the Canada Basin at depths between approximately 50 m and 150 m (Steele et al. 2004) and originates from the Bering Strait inflow. The PWL properties and circulation patterns depend significantly on the wind regime (Fig. 5.20) and sea ice conditions (Fig. 5.16). In 2011, winds tended to push Pacific waters northward and westward (Fig. 5.20, left panel) and there were indications of a PWL winter water signal near the Alpha Ridge in 2011, which was not observed in 2007. This is possibly due to the difference in PWL pathways into the Arctic basins in 2007–10, relative to previous years (Proshutinsky et al. 2011a).

The characteristics of the PWL also depend on water transport through the Bering Strait. Subsequent to the high volume transport of 2007 [~ 1.0 Sverdrup (Sv), similar to 2004], the 2008 volume transport showed a return to approximately the long-term climatology (~ 0.8 Sv), and the data indicate a small increase from that value for 2009 and 2010, with 2010 transports still being below the 2007 maximum. Annual mean tem-

peratures, which showed a step increase of $\sim 1^{\circ}\text{C}$ in 2002, reverted to colder temperatures in 2008 and 2009, with some indication of a warming recurring in 2010. Annual mean salinities increased from 2003 to 2008 and since then have been in a slight decline, but remain higher than 2003 though still less than in 1991. Combined, these changes suggest 2008 and 2009 had modest heat fluxes which were comparable to 2002–03 and 2005–06, while the 2010 heat flux is somewhat

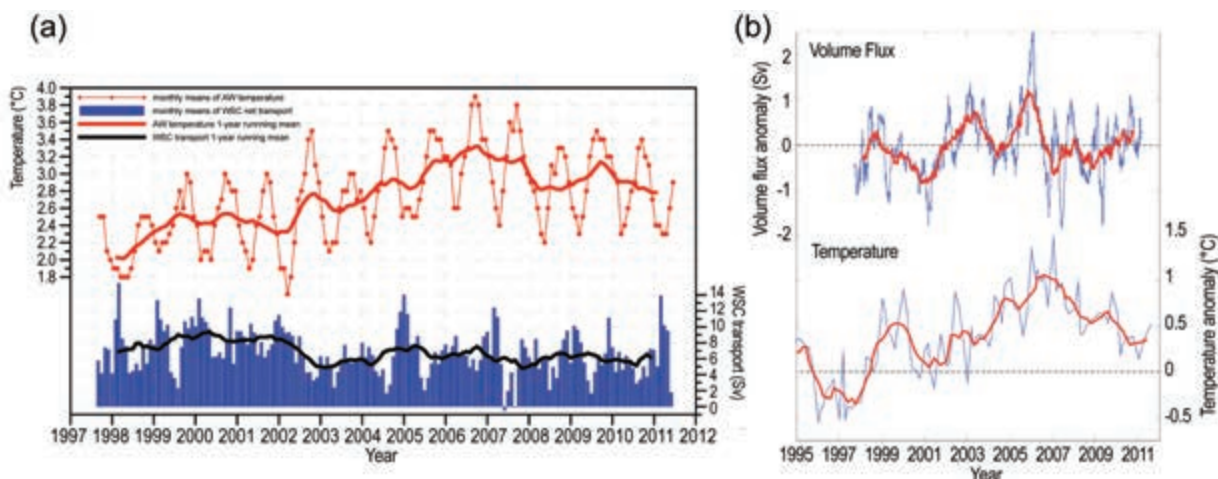


FIG. 5.23. (a) Mean temperature of Atlantic water with a temperature $>1^{\circ}\text{C}$ and the volume inflow in the West Spitsbergen Current, northern Fram Strait, measured by a mooring array at $78^{\circ}50'\text{N}$ maintained since 1997 by the Norwegian Polar Institute and the Alfred Wegener Institute for Polar and Marine Research. **(b, upper panel)** Volume flux anomalies (Sv) in the Atlantic Water with a temperature $>3^{\circ}\text{C}$ in the Barents Sea Opening. The lines show three-month (blue) and one-year (red) moving averages. Anomalies are calculated based on the 1997–2011 mean. **(b, lower panel)** Temperature anomalies in the AWL. The lines show measured values (blue) and 1-year (red) moving average. Anomalies are calculated with respect to the 1997–2006 base period.

higher, similar to 2004 and less than the record high heat flux of 2007. Freshwater flux variability closely resembles volume flux variability, with 2008 and 2009 being less than 2007, and 2010 being closer to the maximum values so far observed in the strait.

3) SEA LEVEL

In 2011, sea level (SL) along the Siberian coast increased relative to previous years. This caused an increase, to $2.66 \pm 0.41 \text{ mm yr}^{-1}$, in the estimated rate of SL rise since 1954 for the nine stations (after correction for glacial isostatic adjustment; Proshutinsky et al. 2004). Until the late 1990s, SL changes were mostly driven by changes of sea level atmospheric pressure (SLP; more than 30% of variability, Proshutinsky et al. 2004) due to the inverse barometer effect. In contrast, from 1997 to 2011, mean SL has generally increased while SLP has remained more or less stable. The tendency toward SL rise in this period may be due to steric effects associated with a reduction of sea ice and ocean surface warming (Henry et al. 2012). After 2008, SL decreased to a minimum in 2010 and then increased in 2011. This variable change likely results from a combination of many forcing factors. One important factor is associated with Ekman transport directed toward coastlines (Fig. 5.20, right panel); in 2011, Ekman transport was responsible for positive sea level anomalies along the Siberian coast.

k. Ocean acidification—J. T. Mathis

Since the Industrial Revolution, rising carbon dioxide (CO_2) levels in the atmosphere and increased absorption by the oceans have created an ocean acidification (OA) phenomenon (e.g., Caldiera and Wickett 2003) that now threatens a number of marine ecosystems (e.g., Fabry et al. 2009). Nowhere is this problem more pronounced than in the highly productive waters of the Pacific Arctic Region (PAR), i.e., the northern Gulf of Alaska, and the Bering, Chukchi and Beaufort Seas. There, mixing processes and colder temperatures naturally precondition the water column to have lower pH and carbonate mineral saturation states (Ω) values compared to more temperate ocean environments.

Data recovered from ocean moorings in 2011 confirm that $p\text{CO}_2$ in bottom waters of the PAR can exceed 1500 μatm for several months each year. This value is well above the threshold for aragonite (a relatively soluble form of calcium carbonate, CaCO_3) undersaturation ($\Omega < 1$) and greater than model predictions of persistent aragonite undersaturation throughout the PAR this century (Steinacher et al. 2009). These recent data are consistent with previous studies that found seasonal aragonite undersaturation occurring in surface and shallow subsurface waters of the PAR at least a decade faster than models predicted (e.g., Caldiera and Wickett 2005).

The PAR is undergoing extraordinary changes in Ω brought on by both natural and anthropogenic

perturbations in an environment that is both sensitive and susceptible to further reductions of Ω (e.g., Mathis et al. 2011). Remineralization of organic matter exported from surface waters due to primary production (see Sidebar 5.3) rapidly increases bottom water $p\text{CO}_2$ over the continental shelves in summer and fall, suppressing pH and Ω . The removal of CO_2 from surface waters by high rates of phytoplankton primary production increases carbonate mineral

concentrations between spring and summer, but these increases are partly counteracted by mixing with sea ice melt water and terrestrial runoff that have low carbonate mineral concentrations. While the processes described above play an important role in conditioning marine waters of the PAR to have naturally low Ω , ocean uptake of anthropogenic CO_2 has shifted Ω values for aragonite below the saturation horizon in broad regions of the continental shelf

SIDEBAR 5.3: ARCTIC OCEAN MARINE ECOSYSTEM RESPONSE TO CHANGING SEA ICE AND OCEAN CONDITIONS—K. E. FREY AND S. E. MOORE

Sea ice breakup and melt during spring influence primary production in the Arctic Ocean and its adjacent shelf seas by enhancing light availability as well as increasing stratification and stabilization of the water column. Dramatic declines in sea ice extent, thickness, and annual duration have recently been associated with significant increases in primary production in several sectors of the Arctic Ocean, in addition to significant shifts in the species composition and timing of phytoplankton blooms.

Newly-compiled satellite observations of primary production in the Arctic Ocean over the period 1998–2009 reveal a ~20% overall increase, resulting primarily from increases in open water extent (+27%) and duration of the open water season (+45 days; Arrigo and van Dijken 2011). However, no statistically significant secular trend in net primary production per unit area was found, stressing the overall importance of sea ice decline in driving the observed trends. Of the eight geographic sectors of the Arctic Ocean investigated by Arrigo and van Dijken (2011), four exhibited statistically significant trends in primary production over this 12-year period: Greenland (-13%), Kara (+70%), Siberian (+135%), and Chukchi (+48%). Frey et al. (2011) additionally show spatially continuous trends in sea ice cover and primary production across the pan-Arctic (Fig. SB5.3). For the Arctic Ocean as a whole, annual phytoplankton primary production averaged $493 \pm 41.7 \text{ Tg C yr}^{-1}$ over the 1998–2009 period (based on direct satellite observations), as opposed to an estimate of $438 \pm 21.5 \text{ Tg C yr}^{-1}$ over the 1979–1998 period (based on linear relationships with open water extent; Arrigo and van Dijken 2011). However, these overall estimates are likely conservative, as they do not account for potential primary productivity that may occur within or beneath sea ice cover.

The community composition of phytoplankton blooms in the Arctic has also shown measurable trends, with recent observations revealing shifts towards a dominance of smaller sized phytoplankton. With a freshening of the Arctic Ocean and associated reduction in the supply of nutrients, trends towards a dominance of smaller picophytoplankton over larger nanophytoplankton have been observed (Li et al. 2009). Even though the total amount of production may not change, a smaller community size structure of primary producers generally may not allow for large transfers of carbon up the food chain.

New observations of the timing of phytoplankton blooms in the Arctic Ocean also show significant changes. Kahru et al. (2010) report significant trends towards earlier phytoplankton blooms for 11% of the area of the Arctic Ocean that could be observed with satellite imagery during the period 1997–2009. Areas experiencing earlier blooms in particular include Hudson Bay, Foxe Basin, Baffin Bay, Greenland coasts, Kara Sea, and near Novaya Zemlya; these are also areas roughly coincident with trends towards earlier sea ice breakup during early summer. In some of these regions, peak blooms in phytoplankton production have advanced from September to early July (a shift of up to ~50 days). Wassmann (2011) also suggests that earlier sea ice retreats cause earlier onsets of the pelagic bloom, thus shortening the growth season of ice algae (which in turn is restricted to occur earlier because of critical limitations of available sunlight). These changes in production were accompanied by biogeochemical shifts in the system, including profound freshening of waters in the Canada Basin and an undersaturation of the surface waters with respect to aragonite, a relatively soluble form of calcium carbonate found in plankton and invertebrates (see section 5k for further information on ocean acidification).

The timing of phytoplankton and/or sea ice algal production is critical for the quantity and quality of primary production and associated grazers and therefore also the transfer of carbon and energy to higher trophic-level species. Specifically, shifts in primary and secondary production have direct impacts on benthic communities (Grebmeier et al. 2010). Organic carbon supply to the benthos in regions of the northern Bering Sea has declined ~30–50%, as has the infaunal biomass of bivalves that are winter prey for the entire world population of the threatened Spectacled Eider. Recent changes in Arctic benthic biodiversity include shifts in community composition and biomass, which may be related to climate warming. In several cases, switches from longer-lived and slow-growing Arctic species and/or communities to faster-growing temperate species and/or communities reflect increasing water temperatures. Similarly, northern range extensions of several sea floor dwellers likely are tied to the warming habitat. In the Atlantic Arctic, this process is anticipated to result in the “Atlantification” of the benthos, i.e., the replacement of Arctic

seas around Alaska, with unknown consequences for marine ecosystems.

Because of the numerous natural and anthropogenic forcing mechanisms, the PAR will serve as a bellwether for the impacts of global ocean acidification in the coming decades as the Arctic and sub-Arctic continental shelves rapidly transition to a new state.

communities with those endemic to the North Atlantic. New research on sediment-associated microbes, including bacteria, archaea, viruses, and microscopic fungi, are currently expanding our knowledge of this topic.

These and other changes in the marine ecosystem are impacting higher-trophic species, including seabirds and marine mammals. For example, 7 of 19 of the world's Polar bear sub-populations are declining in number, with trends in two populations linked to reductions in sea ice (Vongraven and Richardson 2011). For the fourth time in the past five years, thousands of walruses hauled out on the northwest coast of Alaska by mid-August 2011, apparently triggered by a lack of sea ice in the Chukchi Sea (Garlich-Miller et al. 2011). The unprecedented haul-outs on land result in pup mortality by

crushing and a switch in foraging by walrus from moving sea ice to static shore sites. Conversely, the decline in sea ice provides access to waters north of Bering Strait for feeding by seasonally migrant baleen whales. For example, in August 2010, two bowhead whales (one from Alaska and one from West Greenland, each tagged with satellite transmitters) entered the Northwest Passage from opposite directions and spent approximately 10 days in the same area. This is the first time distributional overlap between the two presumed-isolated populations has been documented. Reduced summertime ice in the Northwest Passage (see section 5i) may remove a physical barrier and therefore facilitate genetic exchange between the two populations (Heide-Jørgensen et al. 2012).

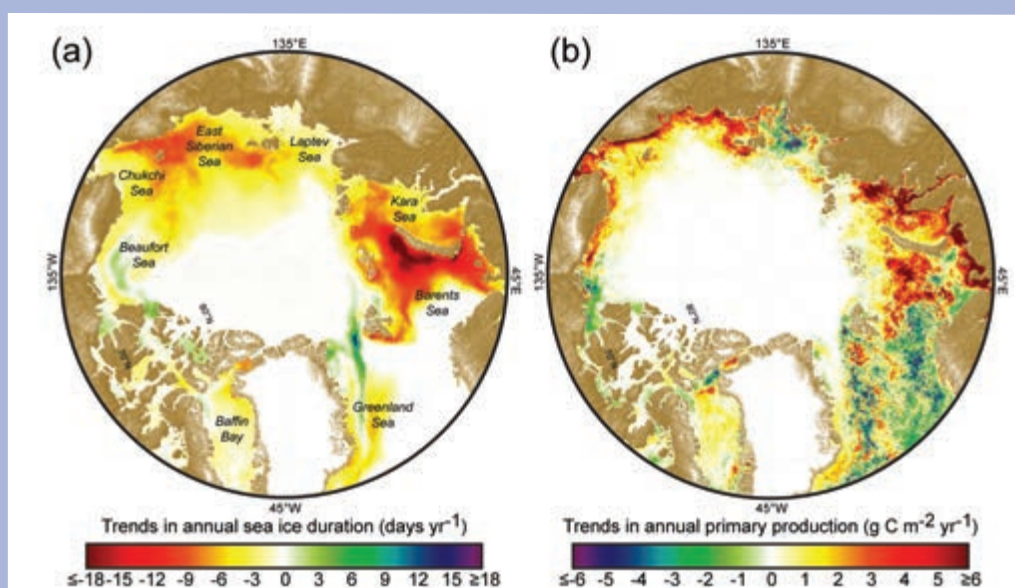


FIG. SB5.3. Trends in annual sea ice duration (days yr^{-1}) and total annual net primary production ($\text{g C m}^{-2} \text{yr}^{-1}$) across the Arctic Ocean and its adjacent shelf seas from 1998 to 2009 (Frey et al. 2011). Annual sea ice persistence data (based on a 15% sea ice concentration threshold) are derived from SSM/I passive microwave radiances (Cavalieri et al. 2008) and primary production data are from Arrigo and van Dijken (2011).